



Universidad
Carlos III de Madrid

Quadrotor UAV for wind profile characterization

Moyano Cano, Javier

Tutor: *García Herrero, Jesús*

Academic advisor: *Fischer, Boris*

University: *Universidad Carlos III de Madrid
Campus de Leganés
Avda. de la Universidad, 30 28911 Leganés, Spain*

Host organization: *Fraunhofer IWES
Institut für Windenergie und Energiesystemtechnik
Königstor 59, 34119 Kassel, Germany*

This project analyzes the idea of wind profile characterization by relating attitude of a quadrotor to local wind profile.

Dedicado a mi familia y amigos

Index	2
Table index	4
Figure index	6
Summary	8
Chapter 1 - Introduction & objectives	10
1.1. Introduction.....	10
1.2. Objectives.....	12
Chapter 2 – Background	14
2.1. Previous projects.....	14
2.2. Sensors for atmospheric wind speed measurement.....	16
2.3. Quadrotor attitude estimation as a measurement system.....	17
2.4. Spatial and temporal scales.....	20
Chapter 3 - Feasibility study	22
3.1. Unmanned Aerial Vehicles.....	22
3.1.1. UAV classification.....	23
3.1.2. Common sensors on board a rotorcraft.....	24
3.2. Attitude estimation.....	27
3.2.1. "Stand alone" sensors.....	28
3.2.2. Data fusion.....	29
3.2.3. Other methods.....	33
3.3. Selecting the platform.....	33
3.3.1. Selection criteria.....	33
3.3.2. Platform comparison.....	34
3.3.3. Selection.....	37
3.4. Flight time.....	38
3.4.1. Electric cable.....	38
3.4.2. Battery.....	39
3.4.3. Weight factor.....	39
Chapter 4 – Model	42
4.1. System model.....	42
4.1.1. Quadrotor model.....	44
4.1.1.1. Motors model.....	44
4.1.1.2. Aerodynamic model.....	46
4.1.1.3. Mechanical model.....	48
4.1.2. Control model.....	52
Chapter 5 – Wind speed calculation	54
5.1. Drag force calculation methods.....	54
5.1.1. Simple method.....	54
5.1.2. Linear equation method.....	54
5.1.3. Kalman filter.....	56
Chapter 6 – Simulations, measurements and tests	60
6.1. Simulations.....	60
6.2. Tests.....	63
6.2.1. Indoor tests.....	64
6.2.2. Outdoor tests.....	64
6.3. Field measurements.....	65
6.3.1. Wind conditions.....	66
6.3.2. No wind conditions.....	70
6.4. Results.....	71
Chapter 7 - Conclusions, limitations & future projects	72

7.1.Conclusions.....	72
7.2.Limitations.....	72
7.3.Future projects.....	73
References.....	74
Appendix & project schedule.....	80

Table index

1- UAV platform comparison.....	15
2- Spatial and time resolution for wind measurement instruments.....	20
3-Unmanned Aerial Vehicle classification.....	23
4- Comparison of sensors in “stand alone” configuration.....	29
5- Platform comparison, according to the selection criteria.....	35
6- Gyroscope technical characteristics.....	36
7- Magnetometer technical characteristics.....	36
8- Barometer technical characteristics.....	36
9- Accelerometer technical characteristics.....	37
10- Comparison between BLDC motors over Glow engines and DC motors.....	44
11- Technical data for BLDC motor AC2830-358, 850 Kv.....	45
12- System model settings.....	60
13- Relative error in % comparing methods.....	61
14- Statistics for wind profile measured by the meteorological mast.....	67
15- Statistics for wind profile estimation.....	71
16- Budget spent in platform, materials and other equipment.....	80
17- Budget spent in human resources.....	80
18-Project schedule.....	81

Figure index

1- Platforms for wind measurement characterization.....	12
2- Common sensors for atmospheric wind speed measurement.....	17
3- Quadrotor scheme.....	18
4- Examples of Unmanned Aerial Vehicles.....	22
5- Detailed view of MEMs gyroscope.....	24
6- Detailed view of 3-axis MEMs accelerometer.....	25
7- 3-axis magnetometer HMC5843.....	26
8- Barometer BMP085.....	26
9- Sonar operating principle.....	26
10- Typical GPS accuracy using WAAS and with SA –on and –off.....	27
11- Roll angle estimation comparison.....	31
12- Operating principle of a LCF for attitude estimation.....	31
13- Operating principle of a LCF for linear position and velocity estimation.....	32
14- Weight ratio between 4 cells and 3 cells commercial LiPo batteries.....	39
15- Propeller angular velocity vs. Battery capacity.....	40
16- Current vs. Battery capacity.....	40
17- Flight time vs. Battery capacity.....	41
18- System model.....	42
19- Quadrotor model.....	43
20- Control model.....	43
21- DC motor model.....	45
22- Relation between Thrust, V_{Bz} and voltage.....	46
23- Aerodynamic model.....	46
24- Quadrotor area estimation.....	47
25- Coefficients k and b for the selected propeller.....	48
26- Mechanical model.....	48
27- Inertial and Body frames of the quadrotor.....	49
28- Model overview.....	53
29- Kalman filter schematic for drag force estimation.....	58
30- Scheme: methods and algorithms validation.....	60
31- Relative error in % comparing methods.....	61
32- Turbulent wind profile generated using Bladed®.....	62
33- Drag and wind speed comparison for turbulent simulated conditions.....	62
34- Figure 32 detailed.....	63
35- Satellite view of the measurement location.....	64
36- Screenshot of the PID setting configuration.....	65
37- Scheme: wind speed calculation.....	66
38- Quadrotor attitude during field measurement.....	67
39- Drag force estimation. Accelerometer data is not filtered.....	68
40- Drag force estimation. Accelerometer data is filtered.....	68
41- Wind speed estimation. Comparison with met mast mean.....	69

42- Wind rose	69
43- Wind speed estimation under no wind conditions	70
44- Wind rose under no wind conditions – Simple method estimation	70
45-Gannt diagram	82

Summary

This project attempts to prove the viability of using an unmanned 4-motors rotorcraft, commonly known as *quadrotor*, as a measurement instrument of wind profiles within large offshore wind farms. The novelty lies in the fact that the vehicle does not include any dedicated sensors for wind characterization, but acts itself as a sensor. This is done by applying an algorithm that relates tilt angle of the vehicle to the local wind speed and direction, sparing the use of external measurement devices such as anemometers, multi-hole probes or any other conventional measurement instrument. Unitary costs and complexity can be consequently significantly reduced. An algorithm for computing wind speed and direction is derived from the dynamic pressure equation, while wind direction is derived from simple trigonometry. As a first approach, wind speed is estimated by solely using the angles computed by the flight controller, dismissing dynamic effects. As a second approach, dynamic linear equations describing the behavior of the quadrotor are used to estimate wind speed, dynamic effects included. In the third approach, wind speed estimation is addressed by using a Linear Kalman Filter (LKF), where dynamic effects are also taken into account. Results coming from each approach are compared to measurement data obtained from an anemometer mounted on a met mast.

Chapter 1

Introduction and objectives

1.1. Introduction

Earth's land has warmed by 1.5 °C over the past 250 years, with humans being almost entirely responsible [1]. Also, new researches demonstrate that recent extreme weather events are a direct consequence of climate change [2]. However, emissions of greenhouse gas keep rising together with the world energy demand, growing exponentially in developing countries. Efficient energy use, together with the exploitation of renewable energy sources are seen as opportunities to fight climate change back and cut dependency on fossil fuel. Among all the renewable resources, wind power positions itself as a leading technology and as a mainstream electricity generation source. Many wind energy projects have been deployed during the last decade, and ambitious designs have been developed by wind power leading companies. In order for the wind energy industry to keep growing, research is being conducted and new wind turbine generation designs have been tested [3]. This new generation maximizes the amount of energy captured by increasing the rotor diameter, which enable the investors to run fewer wind turbines and thus, to reduce the initial investment and the operation and maintenance costs. Upscaling the rotor turbine leads to the following challenges:

- The potential power scales with the square of the rotor diameter, but the blade mass scales to the third power of the rotor diameter. This leads to an increase on the fatigue load of the entire structure, requiring costly structure reinforcements. Alleviation of unwanted loads like this can be achieved by implementing an effective aerodynamic blade load control if a precise description of the incoming wind profile is available.

- Large wind turbines are typically installed forming "clusters", groups containing numerous wind turbines. Wake effects generated by this turbine configuration, combination of at least two wind turbine wakes within the cluster, affect directly the power output and the turbulence intensity, which determines the turbine lifetime. Furthermore, power losses due to wakes can represent between 5 and 20 % of total power output [4]. A better understanding of wake interactions may lead into better predictions of energy production and lower safety factors.

- Commercially available wind turbines installed offshore already reach heights above 200 m, bringing into question the validity of the logarithmic wind profile assumption, valid until a maximum height of 100 m above ground [5]. A better knowledge of the wind shear at these heights would lead into a better use of wind resources for these wind turbines.

In response to the challenges mention above, a deeper knowledge of the wind profile at high altitude and within wind farms is needed. More detailed fatigue life modeling would then be possible, making larger wind turbines feasible, increasing turbine lifetime and at the same time reducing costs. Wind profiles and turbulence intensities have generally been estimated by running very time-consuming simulations. However, further validations are necessary since some of the assumptions applicable for onshore sites are not valid for offshore locations [6]. Furthermore, wind farms with a high number of wind turbines are particularly difficult to model due to wakes interactions. Measurement campaigns have to be conducted in order to improve the understanding of these effects, providing a basis for detailed offshore wind farm wake studies. These measurements can be undertaken either from expensive met masts (a fully equipped offshore meteorology mast could cost many hundred thousand euro) or from portable measurement devices such as sonar or lidar. In any case, the solutions offered by these land-based systems are either expensive or demand certain infrastructure, not necessarily available for offshore measurements [7]. On the other hand, airborne platforms show themselves as a good alternative to land-based systems, being able to take local measurements with high spatial and time resolution. Typical airborne platforms such as tethered balloons and kites have been used for more than a century in atmospheric boundary layer (ABL) research, and manned aerial vehicles (MAV) have carried out multitude of offshore wind measurement campaigns with excellent results. However, these systems are either too big or their movement too unpredictable to use them as measurement platforms within wind farms. Since they are smaller than MAV and more controllable than tethered balloons and kites, unmanned aerial vehicles (UAV) have been recently used for this purpose. Nevertheless, further research must be done in order to clarify their limitations. For this reason, a new measurement approach using a quadrotor as a measurement device is introduced. Quadrotors, a type of UAV, combine several features that give them advantage over conventional measurement devices. In this approach, the UAV acts like a measurement instrument itself, as opposed to conventional UAVs (which carry a dedicated sensor as a payload). The development of UAVs as measurement instruments could make possible to improve the actual knowledge of turbulent wind behavior within a large wind farm, leading into an improvement of the theories that model the wakes interaction and ultimately, extending the turbines lifetime and making the most of the energy provided by the wind.



Figure 1: Platforms for wind measurement characterization. a) Meteorological mast, b) Weather station, c) MAV, d) Tethered balloon, e) Kite, f) UAVs, g) Radiosonde, h) Sodar / lidar / radar

1.2. Objectives

The fundamental objective of this project is to prove the feasibility of using an unmanned aerial vehicle with 4 rotors (*quadrotor*) as a wind measurement instrument itself, without the need of any dedicated sensor for wind profile characterization such as pitot tubes, multi-hole probes or ultrasonic anemometers. Once seen that the system is feasible, minimum spatial and time resolution are derived. In order to do so, a state-of-the-art study must be carried out, considering previous projects using UAVs for meteorological research purposes. It is necessary to select the proper UAV platform, fulfilling the given requirements and to develop algorithms able to compute wind speed and wind direction using the data provided by the selected platform. It is planned to estimate wind speed following three different approaches and to compare their results, to which end subsequent mathematical elaboration and models are needed. First, a system model comprising the dynamic behavior of the quadrotor and its control system must be modeled and second, the three different methods for the wind speed estimation must be developed and implemented in an environment such as MatLab/Simulink®. Connecting the first and the second systems, the validity of the wind speed and direction algorithms can be checked and used for real measurement campaigns.

Chapter 2

Background

Several studies have been carried out, investigating new ways of measuring wind profiles up-, down-stream and within large-scale turbine wind farms. The use of small UAVs has been already considered as an alternative to manned aerial vehicles (MAV) or other conventional platforms for atmospheric wind profiling, such as meteorological masts and active remote sensing systems, mainly based on Lidar and Sodar technologies. New organizations have been created, such as the International Society for Atmospheric Research using Remotely piloted Aircraft (ISARRA), containing data bases with information of atmospheric research airborne platforms, sensors and campaigns conducted during the last years involving UAVs. Furthermore, extensive reports have analyzed the use of different types of UAVs for measurement purposes, comparing accuracy, measurement procedures and data acquisition [4].

2.1. Previous projects

The existing UAV platforms can measure the wind vector either while flying in patterns (fixed wing UAV) or by hovering (rotorcraft UAV). As far as small fixed-wing UAVs are concerned, the question of which flight patterns are best for which investigations has not been answered yet, and it is still uncertain how to effectively compare measurements along a flight path with measurements from a fixed mast. On the other hand, rotorcraft UAVs' strong point is their ability to measure wind speed and direction at a fixed position in space, making it easier to compare results. Until now, small UAVs were equipped with meteorological sensors, which increases the minimum payload capacity required by the vehicle and shorten their flight time. Concerning small rotorcrafts, it is known that the downwash reaches its maximum velocity at a distance of 2-3 times the rotor diameter while hovering, interfering with the incoming wind vector and affecting the measure. The following are recent studies using UAVs as wind measurement devices:

- **SUMO:** The Small Unmanned Meteorological Observer is a platform based on a light-weighted Styrofoam model airplane, partially developed by the University of Bergen, Norway. It is equipped with temperature, humidity and pressure sensors and the attitude is controlled by the Paparazzi autopilot system. It measures wind speed and direction by following a helical flight pattern, typically used for boundary layer profiling. The on-board GPS measures the instant ground speed for the descending part of the spiral. The ground speed is decelerated when flying headwind, and accelerated

when flying tailwind, making possible to calculate the horizontal wind speed and direction by using these ground speed differences [8].

- ***M²AV***: The M²AV (Meteorological Mini Unmanned Vehicle) is based on the unmanned 'Carolo T200' aircraft, developed by Mavionics GmbH in collaboration with the University of Braunschweig, Germany. It measures the wind vector with a five-hole probe mounted on the fuselage nose together with an extra IMU and GPS system, getting a spatial resolution of turbulence measurements in the sub-meter range. The attitude is controlled by using a GPS and an IMU shield. 'MINC' is the autopilot system, also developed by the University of Braunschweig. It took part on several scientific missions, among them the LAUNCH campaign and a mission in Antarctica at the British Antarctic Survey station Halley [9].

- ***MASC***: The Multi-purpose Automatic Sensor Carrier is a platform based on a small UAV airplane (5 kg) able to operate automatically. It took part on the BLLAST project, which attempts to get a better understanding of the atmospheric boundary layer (ABL) structure and how it changes between daytime convective ABL and nighttime stable ABL [10]. It measures flux momentum, heat and humidity along straight flight paths at constant speed and several altitudes. The meteorological sensor equipment is very similar to the M²AV.

- ***Vario XLC***: Vario XLC platform is based on a small-sized helicopter from the company Vario. Its high payload capacity makes possible to install a rather heavy and more accurate sensor, in this case a 3D sonic anemometer, attached to the helicopter by means of a 4-5 meters wire as a slung load. The anemometer swings and rotates during the flight, so an inertial navigation system (INS) was attached to the load in order to estimate its attitude and thus, the true wind speed and direction.

Table 1: UAV platform comparison

	Platform			
	<i>SUMO</i>	<i>MASC</i>	<i>M²AV</i>	<i>VarioXLC</i>
Developer	Bergen University	Tübingen University	Braunschweig University	Aalborg University
Vehicle	Fixed wing UAV	Fixed wing UAV	Fixed wing UAV	Helicopter UAV
Max. take-off weight	580 g	4000 g	6000 g	40000 g
Payload	140 g	1000 g	1500 g	4000 g
Sensors on board (parameter)	Sensirion SHT 75 (temperature and humidity) VTI SCP1000 (Pressure) MLX90247 (Surface temperature) Eagle Tree Pitot tube (1-D flow vector) 5 hole probe, Aeroprobe (3-D flow vector)	Vaisala HMP 50 (temperature and humidity) Termocouple type-k (temperature) 5 hole probe (3-D flow vector)	Vaisala HMP 50 (temperature and humidity) Termocouple type-k (temperature) 5 hole probe (3-D flow vector)	3-D ultrasonic wind sensor (3-D flow vector)
Max. flight time	< 30 min	1.5 h	> 45 min	30 min

2.2. Sensors for atmospheric wind speed measurement

This section gives a short overview of the most common sensors and systems used to characterize boundary layer winds and turbulent flows, emphasizing its applicability on board small UAVs.

Cup anemometers: These instruments, able to measure wind speed, consist of a number of cups mounted with vertical arms on a rotating shaft. They are the standard sensors used for wind assessment and thus, all other wind speed measurement methods are compared to its accuracy. Cup anemometers' accuracy is sensitive to vertical velocity components. However, in theory it would be feasible to mount them on board a small rotorcraft UAV. Its verticality could be controlled, for instance, by attaching it to a 3-axis gimbal system.

Propeller anemometer: This instrument uses a propeller mounted on a horizontal axis to measure wind speed. It is often combined with a wind vane so the propeller always keeps facing the wind, making possible to measure both wind speed and direction. Miniaturization of these sensors could be mounted on top of a small UAV.

Sonic anemometer: Sonic anemometers measures wind speed and direction based on the time of flight of sonic pulses between pairs of transducers, being able to measure a 3-dimensional flow. It is one of the most accurate sensors for wind profile characterization together with the hot-wire anemometer. However, the presence of dust or sea spray worsens its performance. They have already been tested attached to small UAVs [11].

Hot-wire anemometer: These sensors use an electrically heated fine wire to measure wind speed. The air flowing past the wire has a cooling effect on the wire. By relating the electrical resistance of the wire to its temperature, the wind speed can be obtained. They have a very high frequency response, making them especially suitable for the study of turbulent flows. They fit on small UAVs but unfortunately they are too fragile to resist a collision with the ground.

Sphere anemometer: This sensor relates the drag force acting on a sphere mounted on the tip of a rod to the rod's bending moment, getting this way wind speed and direction. Its temporal resolution is limited by the resonance frequency of the rod. The use of these type of anemometers on board small UAVs seems feasible.

Laser-cantilever anemometer: This new instrument uses a laser and a position sensitive detector to determine the deflection of the tip of a micro cantilever. The deflection is caused by the drag force of the wind acting on the cantilever. Its high frequency response makes it suitable for turbulent flows [12]. Due to its weight the use of these sensors together with small UAVs is still not possible.

Pitot tube: This instrument uses Bernoulli's equation to relate wind speed to static and total pressure of the incoming air flow. It consists of a tube pointing into the fluid flow.

The moving flow stagnates, giving a value of the total pressure. The static pressure is measured using an additional hole located at the side of the tube. The dynamic pressure can then be calculated and thus, the wind speed. Its limitation is the necessity of being pointed directly into the fluid flow. However, they can be used mounted on the fuselage nose of a small aircraft UAV.

Multi-hole probe: These sensors extend the operating principle of Pitot tubes to 3 dimensional flow measurements by using several holes at the tip of the probe. Recent projects have developed a miniaturization of a 7-hole probe [13]. making possible to mount them on board a small UAV.

Sodar, Lidar and Radar: These active remote systems uses the Doppler shift of emitted sound waves (Sodar) or electromagnetic waves (Lidar and Radar) reflected by density inhomogeneities (Sodar and Radar) or aerosol particles (Lidar) suspended in the air to characterize the wind profile. All existing systems are too heavy to be used on board a small UAV.



Figure 2: Common sensors for atmospheric wind speed measurement. From left to right and from top to bottom: Cup anemometer, propeller anemometer, sonic anemometer, hot-wire anemometer, sphere anemometer, laser-cantilever anemometer, pitot tube, multi-hole probe, sodar, lidar and radar

2.3. Quadrotor attitude estimation as a measurement system

This project attempts to prove the feasibility of using a small quadrotor UAV to measure wind speed and direction without the use of any atmospheric wind measurement sensor. When the quadrotor hovers at a certain position in space, the drag force of the wind acting on it tends to push it. If the autopilot system forces the quadrotor to keep the position the quadrotor will tilt, compensating the drag force with a horizontal component of the thrust force generated by the rotors. The stronger the wind, the more tilted the quadrotor. Under steady state conditions, it is straight forward to estimate the wind vector by knowing the drag coefficient of the vehicle and the area exposed. These values can be found out by doing a wind tunnel test. The following equation, which can be derived from the conservation of energy for a fluid in motion, shows how to estimate wind speed [14]

$$\mathbf{v} = \sqrt{\frac{2D}{\rho A(\gamma) C_D(\gamma)}}$$

where \mathbf{v} is the wind speed in [m/s], D denotes the Drag force acting on the quadrotor in [N], ρ is the air density at the measurement point in [kg/m³], $A(\gamma)$ denotes the area exposed to the incoming wind in [m²] as a function of the quadrotor angle (γ) and $C_D(\gamma)$ is the drag coefficient, also function of the quadrotor angle. It is worth mentioning that γ is a combination of two of the Euler angles roll (ϕ) and pitch (θ). Using the attitude estimation of the vehicle, these two angles (together with the third Euler angle yaw (ψ)) are known, making possible to also estimate the wind direction. The following figure shows how roll and pitch Euler angles are related to the tilt angle.

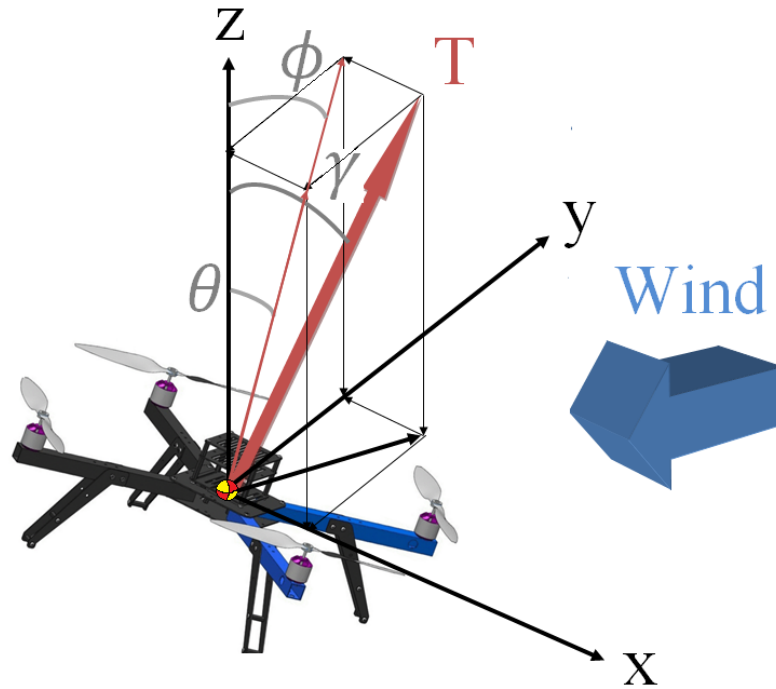


Figure 3: Quadrotor scheme. Quadrotor tilts when wind generate a drag force. Tilt angle is combination of roll and pitch Euler angles in the inertial frame of references (x,y,z)

The following equation relates tilt angle (γ) to roll (ϕ) and pitch (θ) angles:

$$\gamma = \cos^{-1}\left(\frac{\vec{n}_{XY} \cdot (\vec{e}_\phi \times \vec{e}_\theta)}{|\vec{n}_{XY}| \cdot |\vec{e}_\phi \times \vec{e}_\theta|}\right) \quad \text{with} \quad \vec{e}_\phi = \begin{pmatrix} 0 \\ \cos\phi \\ \sin\phi \end{pmatrix} \quad \text{and} \quad \vec{e}_\theta = \begin{pmatrix} \cos\theta \\ 0 \\ -\sin\theta \end{pmatrix}$$

where \vec{n}_{XY} is the unit vector $\begin{pmatrix} 0 \\ 0 \\ 1 \end{pmatrix}$ normal to the XY-plane.

Wind direction can be calculated following the next steps:

- First, calculate the angle λ between the direction of the quadrotor and the projection of the vector $(\vec{e}_\phi \times \vec{e}_\theta)$ on the XY-plane

$$\lambda = \psi - \text{atan} \left(\frac{(\vec{e}_\phi \times \vec{e}_\theta)_Y}{(\vec{e}_\phi \times \vec{e}_\theta)_X} \right)$$

where ψ denotes the yaw angle in [rad] and $(\vec{e}_\phi \times \vec{e}_\theta)_X$ and $(\vec{e}_\phi \times \vec{e}_\theta)_Y$ are the projection of the cross product on the X- and Y-axis, respectively.

- Second, determine whether the projection of the cross product $\vec{e}_\phi \times \vec{e}_\theta$ on the XY-plane is on the left or on the right side of the quadrotor

$$\vec{n}_{XZ} \cdot (\vec{e}_\phi \times \vec{e}_\theta)_{XY} = \begin{cases} < 0, & \text{if } \vec{e}_\phi \times \vec{e}_\theta \text{ is left} \\ > 0, & \text{if } \vec{e}_\phi \times \vec{e}_\theta \text{ is right} \\ = 0, & \text{otherwise} \end{cases}$$

- Lastly, the wind direction can be calculated as follows

$$\text{Wind direction} = \begin{cases} (360^\circ - \lambda + \psi), & \text{if } \vec{n}_{XZ} \cdot (\vec{e}_\phi \times \vec{e}_\theta)_{XY} > 0 \\ (\lambda + \psi), & \text{if } \vec{n}_{XZ} > 0 \end{cases}$$

However, the measurement of wind profiles in turbulent environments (for instance behind and between large wind turbines) is more interesting. Under this condition the steady state assumption is no longer valid and dynamic effects should be considered. The inertia of the vehicle, together with its linear and rotational acceleration and velocity has to play an important role in the new wind vector estimation. Three different approaches have been followed

- **First approach:** In the first approach dynamic effects have been disregarded. Drag force acting on the quadrotor has been calculated only using the Euler angles provided by the attitude estimation algorithm implemented in the quadrotor.

- **Second approach:** The second approach is to directly calculate the drag force by using the linear dynamic equations that characterize the behavior of an ideal quadrotor. The inputs for the equation come also from the quadrotor attitude estimation algorithm and from the sensors on board.

- **Third approach:** Finally, the drag force is estimated taking into account linear velocities of the quadrotor by using a Linear Kalman Filter (LKF). The inputs of the filter come from the quadrotor attitude estimation algorithm and from the sensors on board.

Sensors do not have infinite accuracy and there are always errors present in the measurements output data. While the second approach estimates the wind without taking into account these errors, the third approach is able to take them into account by

using the LKF. After estimating the drag force, the wind vector is calculated following the equation above. The area exposed is calculated through the Euler angles, provided by the attitude estimation algorithm and the drag coefficient $C_D(\gamma)$ is assumed to be constant with a value of 0.9 (same as an angled cube).

2.4. Spatial and temporal scales [15]

Each measurement instrument has different spatial and temporal resolutions, making them especially suitable for certain wind conditions. The table below resumes the characteristics of the measurement instrument analyzed in *Section 2.2.*, showing minimum values for time and spatial resolution.

Table 2: Spatial and time resolution for wind measurement instruments

		Time resolution							
		1000 Hz 0.001 s	100 Hz 0.01 s	10 Hz 0.1 s	1 Hz 1 s	0.1 Hz 10 s	0.01 Hz 100 s	0.001 Hz 1000 s	0.0001 Hz 10000 s
Spatial resolution	0.01 m	Hot-wire anemometer		Pitot tube Multi-hole probe					
	0.1 m	Laser-cantilever anemometer	Sonic anemometer	Sphere anemometer	Cup anemometer Propeller anemometer				
	1 m			Quadrotor ^a	Lidar				
	10 m								
	100 m				Wind turbine				
	1000 m					Wind farm			
	10000 m								

^a Spatial and time resolution estimation.

Chapter 3

Feasibility study

The following sections introduce the concept of Unmanned Aerial Vehicle, its classification and a description of the sensors mounted on board. Different attitude estimation methods are explained, putting emphasis on the methods based on data fusion algorithms. Next, available platforms are compared, selecting the most convenient for the purposes of the project. Maximum flight time is also estimated.

3.1. Unmanned Aerial Vehicles

An Unmanned Aerial Vehicle, better known as UAV, is an aircraft able to fly without a human pilot, controlled either autonomously or under remote control. They perform a wide variety of functions, most of them related to remote sensing. In the past decade unmanned aerial vehicles have become a topic in many research organizations, finding application in many areas such as search and rescue services, traffic surveillance, preventive maintenance, meteorological services, agriculture and military espionage, among others. Furthermore, during the last years micro UAVs have become very popular among radio control hobbyist, and the number of open source projects have been increased on the internet, making it easier for researchers to use them and to modify hardware and software at will, fitting their necessary requirements.



Figure 4: Examples of Unmanned Aerial Vehicles. From left to right: Hexacopter, MALE RQ-1 Predator and NAV "Nano Hummingbird" (flapping-wing UAV configuration)

3.1.1. UAV classification

The literature is mainly oriented towards military applications and classifies the UAVs by the capability or size of the air vehicle that is required to carry out a particular mission [16]. They can also be categorized in terms of functionality, range/altitude limits and airframe type. The next table categorizes the unmanned vehicles relating weight, range and altitude:

Table 3: Unmanned Aerial Vehicle classification [17]

Class	Category	Normal operating altitude	Normal mission radius
Class I (less than 150 kg)	Small UAV > 20 Kg	Up to 1500 m AGL ^a	50 km (LOS) ^b
	MUAV (Mini UAV) 2-20 Kg	Up to 1000 m AGL	25 km (LOS)
	MAV (Micro UAV) 0.1 - 20 Kg	Up to 60 m AGL	5 km (LOS)
	NAV (Nano UAV) < 100 g	Up to 10 m AGL	500 m (LOS)
Class II (150 Kg to 600 Kg)	TUAV (Tactical UAV)	Up to 3000 m AGL	200 km (BLOS) ^c
Class III (more than 600 Kg)	STRIKE/COMBAT	Up to 20000 m AGL	Unlimited (BLOS)
	HALE (High altitude long endurance)	Up to 20000 m AGL	Unlimited (BLOS)
	MALE (Medium altitude long endurance)	Up to 14000 m AGL	Unlimited (BLOS)

^a - Above-Ground-Level

^b - Line-of-Sight

^c - Beyond-Line-of-Sight

Regarding airframe types, there are 4 basic configurations, i.e. fixed-wing, rotary-wing (known as rotorcraft), flapping-wing (*Figure 4*) and lighter-than-air configuration. Among these, rotorcrafts with 4 rotors, commonly known as quadrotors, are growing in popularity, becoming a standard platform for robotics researchers worldwide. The main reasons for this are:

- They have already proven to be highly maneuverable [18], making them useful in all kind of situations and environments [19].

- They are economic and available in a high variety of sizes.

- Its mechanical design is relatively simple.
- They are inherently unstable, representing a challenging example of a safety critical embedded real time system.
- Recent improvements of battery and other technology like MEMs is rapidly increasing the scope for commercial opportunities [20].

3.1.2. Common sensors on board a rotorcraft

A rotorcraft typically consists of four, six or eight individual rotors attached to a rigid cross airframe. Control of a rotorcraft is achieved by differential control of the thrust generated by each rotor. In order to do so it is necessary to estimate the vehicle state, i.e. its height, attitude, angular velocity and linear velocity, being attitude and angular velocity the most important as they are the primary variables used in attitude control of the UAV. The most basic instrumentation needed is an Inertial Measurement Unit (IMU). The IMU typically includes a 3-axis rate gyroscope, 3-axis accelerometer and 3-axis magnetometer, whose outputs are usually converted from analog to digital information through an analog-to-digital converter (ADC), whose resolution will determine the accuracy of the instrument (the higher, the more accurate the measurement). In addition, most rotorcrafts include a barometric sensor for determining relative height, a GPS as an extra sensor to measure absolute position and a sonar. Laser-ranging or infrared sensors can also be implemented. The basic sensors are described below.

- **Gyroscope:** These sensors are one of the most relevant for air vehicle navigation and control, along with accelerometers. Traditional units have been usually expensive and bulky, but with the maturation of semi-conductor manufacturing technology, microelectro-mechanical sensors (MEMS) applications have shifted to non-military purposes, making MEMS gyroscopes cheaper and smaller and thus, more suitable for flight attitude calculations on board UAVs [21]. Neither their classification nor their physics are here discussed; a good source can be found in [22], [23] and [24]. Basically, a rate gyro measures the angular velocity of $\{\mathbf{B}\}$ relative to $\{\mathbf{A}\}$ expressed in the body frame of reference $\{\mathbf{B}\}$

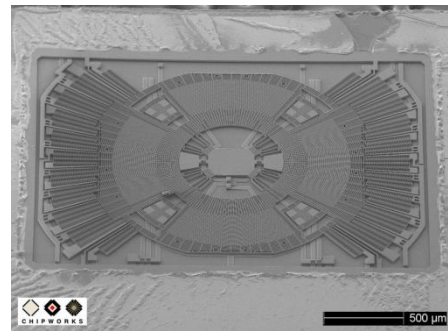


Figure 5: Detailed view of MEMS gyroscope

$$\Omega_{IMU} = \Omega + \mathbf{b}_\Omega + \eta_g \in \{\mathbf{B}\}$$

where Ω_{IMU} denotes the true angular velocity of the IMU in $[\text{°}/\text{s}]$, Ω is the angular velocity measured by the gyroscope in $[\text{°}/\text{s}]$, η_g denotes the additive measurement noise and \mathbf{b}_Ω denotes a slowly time-varying gyro bias (usually considered as a constant) caused by manufacturing limitations, both in $[\text{°}/\text{s}]$ units. The calculation of attitude angles requires angular velocity measurements for integral calculation. The gyro bias

shows itself after integration as an angular drift, leading to decrease accuracy, causing basic limitations to solely using gyroscopes for attitude estimation [21].

In practice a gyroscope will rarely output values expressed in °/s. Digital gyroscopes will output the information using a serial protocol like I2C, SPI or USART, while analog gyroscopes will output a voltage level within a range, which will have to be converted to a digital value through an ADC. In order to turn this raw data into °/s units the following equation can be used

$$\begin{pmatrix} \hat{R}_x \\ \hat{R}_y \\ \hat{R}_z \end{pmatrix} = \begin{pmatrix} 1/S_{gx} & 0 & 0 \\ 0 & 1/S_{gy} & 0 \\ 0 & 0 & 1/S_{gz} \end{pmatrix} \begin{pmatrix} R_{rx} - R_{x0} \\ R_{ry} - R_{y0} \\ R_{rz} - R_{z0} \end{pmatrix}$$

where \hat{R}_x , \hat{R}_y and \hat{R}_z are the estimated angular rates for each axis in [°/s], S_x , S_y and S_z the sensitivity scale factors for each axis in [LSB/(°/s)], R_{rx} , R_{ry} and R_{rz} the MEMS gyroscope raw measurements for each axis in [LSB] and R_{x0} , R_{y0} and R_{z0} the zero-rate-levels for each axis in [LSB]. All these parameters can be found generally in the datasheet, provided by the sensor manufacturer.

- **Accelerometer:** This inertial sensors are electromechanical devices that measure the instantaneous linear acceleration of $\{\mathbf{B}\}$ due to external forces, either static (like the constant force of gravity) or dynamic (caused by moving the accelerometer), being a very common way to do so by sensing changes in capacitance [25]. They are described by the following equation:

$$a_{IMU} = R^T(\dot{v} - g\vec{z}) + b_a + \eta_a \in \{\mathbf{B}\}$$

where a_{IMU} is the true acceleration of the IMU in [m/s²], \dot{v} is the external acceleration in the inertial frame in [m/s²], R^T is the rotation matrix transpose, $g\vec{z}$ represents the magnitude and direction of the gravitational acceleration in [m/s²], b_a denotes a bias term and η_a is the additive measurement noise, both in [m/s²].

A 3-axis accelerometer will give an accurate orientation of a stationary platform relative to the Earth's surface; however, when the platform starts moving (or vibrating) it will be subjected to a new acceleration, which will be added to the acceleration vector provided by gravity, making hard to distinguish between gravity force and other exogenous forces. Typically, the acceleration components caused by the dynamic movements of the robot only happen in a short period of time, while gravity acceleration is acting on the UAV permanently. By low-pass filtering the data from the accelerometer, unwanted high frequency acceleration components can be filtered out; however, the low-pass filter will slow-down the response time of the measurement [26]. Furthermore, ordinary accelerometer configurations are not able to measure movements orthogonal to gravity (i.e. yaw angles), even though there are ways to achieve this by combining two 1-axis accelerometers [27]. Just like gyroscopes, accelerometers can be categorized as analog or digital devices, depending on the output

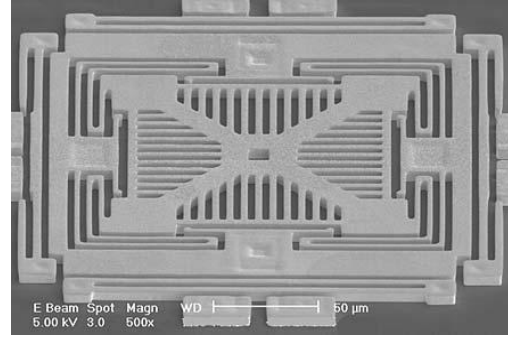


Figure 6: Detailed view of 3-axis MEMS accelerometer

units, and an ADC is also used to produce the final raw data. A similar equation is used to turn raw data coming from the ADC into acceleration units

$$\begin{pmatrix} \hat{a}_x \\ \hat{a}_y \\ \hat{a}_z \end{pmatrix} = \begin{pmatrix} 1/S_{ax} & 0 & 0 \\ 0 & 1/S_{ay} & 0 \\ 0 & 0 & 1/S_{az} \end{pmatrix} \begin{pmatrix} a_{rx} - a_{x0} \\ a_{ry} - a_{y0} \\ a_{rz} - a_{z0} \end{pmatrix}$$

where \hat{a}_x , \hat{a}_y and \hat{a}_z are the estimated accelerations for each axis in [m/s²], S_{ax} , S_{ay} and S_{az} the sensitivity scale factors for each axis in [LSB/(m/s²)], a_{rx} , a_{ry} and a_{rz} the MEMS accelerometer raw measurements for each axis in [LSB] and a_{x0} , a_{y0} and a_{z0} the zero-rate-levels for each axis in [LSB].

- **Magnetometer:** These sensors are able to measure the Earth's magnetic field vector. The following equation is used to estimate the true magnetic field:

$$m_{IMU} = R^T A_m + B_m + \eta_m \in \{\mathbf{B}\}$$

where m_{IMU} is the estimation of the magnetic field in [gauss], R^T is the rotation matrix transpose, A_m is the

Earth's magnetic field vector in [gauss] (expressed in the inertial frame), B_m is a body-fixed frame expression for the local magnetic disturbance and η_m denotes the measurement noise, both in [gauss]. As the expression shows, magnetometers are also subjected to interferences, such as magnetic fields resulting from motor windings.



Figure 7: 3-axis magnetometer HMC5843

- **Barometer:** Barometer sensors are devices able to measure atmospheric pressure. The equation relating altitude with pressure and temperature for dry air is known as the hypsometric equation. Assuming zero lapse rate (constant temperature with elevation) the equation that estimates the altitude takes the following form:

$$h_1 = -\frac{RT}{g} \log\left(\frac{p_1}{p_0}\right) + \eta_b$$

where h_1 is the estimated absolute height in [m], R is the air specific gas constant in [J/(KgK)], T denotes the average temperature in the layer $p_1 - p_0$ in [K], g is the gravity acceleration in [m/s²], p_1 is the measured pressure in [Pa], p_0 is the pressure at zero altitude in [Pa] and η_b denotes the measurement noise in [m]. Current commercial barometers like those used in small UAVs have an altitude resolution down to several centimeters.

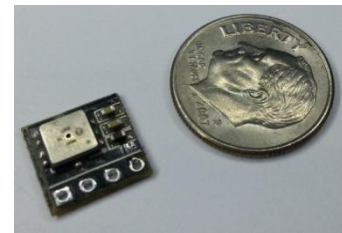


Figure 8: Barometer BMP085

- **Sonar:** A sonar sensor is a device that uses sound propagation to detect objects in the surroundings. When the device comes with a transmitter and a receiver it is called "active" sonar, which are generally the ones used on board small UAVs. They create a pulse of sound and

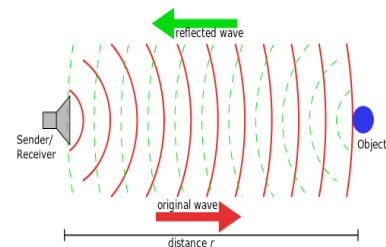


Figure 9: Sonar operating principle

then they listen for reflections of the pulse. To measure the distance from the transmitter to an object, the time transmission of a pulse to reception is measured and converted into a range by knowing the speed of sound, as shown in equation:

$$r = v_s \frac{t}{2} + \eta_s$$

where r denotes the distance in [m] from the transmitter to the object, v_s is the speed of sound in air in [m/s], t is the time transmission in [s] and η_s denotes the measurement noise in [m]. Sonar sensors operating during flight onboard quadrotors have to deal with several sources of noise, among them air turbulence, acoustic noise caused by the propellers and electrical noise caused by the driven motors. These issues can be solved by mounting the sensor as far from the propellers as possible and filtering the output signal through a low-pass filter [28]. Commonly commercial sensors for civilian uses detects objects from 0.02 to 8 meters with 0.01 m resolution [29].

- **GPS receiver:** This type of sensors uses the Global Positioning System, a satellite-based navigation system that sends and receives radio signals. It provides information about current location in all weather conditions in an unobstructed line of sight to four or more GPS satellites. GPS accuracy varies from a few meters to a hundred meters, depending on its configuration. *Figure 10* shows typical accuracies for SA mode on and off, and by using WAAS accuracy (EGNOS satellite-based augmentation system is used in Europe instead of WAAS).

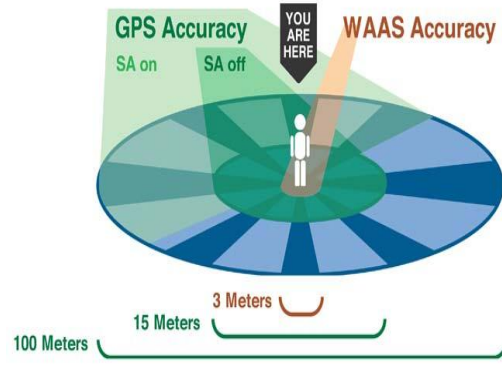


Figure 10: Typical GPS accuracy using WAAS and with selective availability (SA) -on and -off

3.2. Attitude estimation

Within the algorithm introduced in *Section 2.3.*, two terms are dependent on the attitude, i.e. drag coefficient $C_D(\gamma)$ and area exposed $A(\gamma)$. As a result, a good estimation of the attitude is needed. There are a few ways to achieve this, namely:

- **“Stand-alone” sensors:** Sensors such as gyroscopes, accelerometers or magnetometers in "stand-alone" configuration could be used. However, they lack accuracy either in the long term or in the short term. Furthermore, the reliability improves when the system depends not only on one type of sensor but on a combination of them. If at any given time a particular sensor fails, the rest can manage to keep the system stable.

- **Data fusion:** Fusing the information coming from different sensors to get a better estimation of the attitude. There are several algorithms that perform data fusion, among them the Kalman filter (KF) in its different versions (linear KF, extended KF and unscented KF) and the complementary filter (CF) also in its linear (LCF) and non-linear (NCF) version. The difference between KF and CF is briefly shown in *Section 3.2.2.*

- **Alternative methods:** Making use of devices which are not meant to be used as attitude sensors. For instance, relating motors power consumption to Euler angles. Micro voltmeters and ammeters can provide a direct and accurate observation of the required parameters.

The following will give a brief introduction and examples to the attitude estimation methods mentioned above.

3.2.1. "Stand-alone" sensors:

Gyroscopes: Since these sensors detect the rotation rate of a body, a simple integration in time gives the angle the body has assumed. Consequently, the use of three gyroscopes, each of them aligned with the body frame axis, would provide the final attitude of the body. In practice, the time is discretized into time steps during which rotation speed is assumed to be constant. The angle at time t_1 is

$$\alpha_1 = \Omega(t_1 - t_0)$$

where Ω denotes the gyroscope measurement in [°/s] and $(t_1 - t_0)$ is the timestep length in [s]. As mentioned before, gyroscopes have a noise term and a bias term that when integrated over long time end up on attitude errors in the order of several degrees [30]. Furthermore, the bias term is not constant but rather it varies over time. Even though there are ways to get over major error sources in MEMS gyroscopes [31], a minimal-drift term remains. As a result, estimating the attitude using a 3-axis gyroscope alone will give good results just in the short term.

Accelerometers: Assuming that the gravitational acceleration is the only given acceleration, it is possible to partially estimate the attitude by computing the Euler angles from the accelerometer output. The use of 2 accelerometers with their axis aligned with the roll and pitch axis of rotation will give the pitch and roll angles, respectively. Accelerometers cannot measure the third Euler angle, yaw, since they are insensitive to rotations around the earth's gravitational field vector. Nevertheless, an extra sensor with its axis pointing along the gravitational vector can be used, after two integrations, to estimate the vertical position. Assuming no acrobatic flights, calculation of roll and pitch angles is straightforward by using simple trigonometry

$$\theta = \sin^{-1}(a_x)$$

$$\phi = \sin^{-1}\left(\frac{a_y}{\cos\theta}\right)$$

where a_x and a_y are the accelerometer output, normalized with the gravitational acceleration constant g . In practice, the accelerometer is subjected to additional accelerations caused by vibrations or other external forces. The accelerometer cannot distinguish between gravitational acceleration and the rest, losing its reference and giving wrong attitude estimation. However, accelerations other than gravitational acceleration occur only during short periods of time, making 3-axis accelerometers a good attitude estimator in the long term.

Magnetometers: These sensors detect the Earth’s magnetic field and define a 3-dimensional magnetic vector. This vector can be used as a reference to determine the heading (yaw) of the vehicle. Any rotation around this vector will be unknown, making the sole use of 3-axis magnetometer not suitable for a complete attitude estimation.

GPS: This system alone cannot be used to determine the attitude of a UAV, since they do not detect rotations around the body frame of reference. However, the relevance of the GPS lies in its use to determine the absolute position of the UAV (translational velocity could also be obtained by deriving position over time). However, they cannot be used solely due to its slow update rate (1 - 10 Hz). Furthermore, vertical accuracy is typically 5 times worse than horizontal accuracy, making them not so reliable for altitude estimation. Barometers can be used for this purpose instead.

The next table gives a schematic overview of the advantages and disadvantages of solely using the sensors described above, while at the same time gives an idea of how to combine them.

Table 4: Comparison of sensors in “stand-alone” configuration for position and attitude estimation

Sensor	Measurement	Attitude estimation	Translational velocity estimation	Horizontal position estimation	Vertical position estimation	Advantages	Disadvantages
Accelerometer	Accelerations	PITCH ROLL	POOR	POOR	POOR	Long term accuracy	Vulnerable to vibration
Gyroscope	Angular rates	PITCH ROLL YAW	NO	NO	NO	Short term accuracy	Suffers from drift.
Magnetometer	Magnetic fields	YAW	NO	NO	NO	Fixed reference	Vulnerable to external magnetic disturbances
Gps	Absolute positions	NO	YES	YES	POOR	Fixed reference	Vertical accuracy, only outdoors.
Barometer	Absolute height	NO	NO	NO	YES	Absolute height, vertical accuracy.	Vulnerable to pressure disturbances, range up to 10 meters.
Sonar	Relative height	NO	POOR	NO	YES	Very accurate for	

3.2.2. Data fusion

The ideal way of estimating the attitude of a vehicle goes through combining the information provided by its sensors in a way that the advantages of some make up for the lacks of the others. Three methods are described here, corresponding to the attitude estimation algorithms used by the UAV platforms considered in *Section 3.3.2*.

3.2.2.1. Linear Kalman Filter [32]

This algorithm is used to estimate the *system state* of a *linear dynamic system*

(perturbed by *Gaussian white noise*) using *measurements* that are linear functions of the *system state* (also corrupted by additive Gaussian noise). Applying this definition to a quadrotor, the *system state* defines the system's varying quantities (for example the linear and angular position and velocity of the vehicle), the *linear dynamic system* is a representation of the physical laws that describe the system (the linear and angular equations describing the dynamic behavior of the vehicle) and the *measurements* are the available information observed over time (the output data coming from the multiple sensors on board the UAV).

In discrete-time a linear dynamic system and the observations can be described as follows

$$\begin{aligned} x_k &= F_k x_{k-1} + B_k u_k + w_k & ; & & w_k &\sim \mathcal{N}(0, Q_k) \\ z_k &= H_k x_k + v_k & ; & & v_k &\sim \mathcal{N}(0, R_k) \end{aligned}$$

where x_k and z_k are the state estimate and the observation vector respectively, F_k denotes the so called *state transition model*, H_k is the *observation model*, x_{k-1} the *previous state estimate*, B_k the *control-input model*, u_k the *control vector* and w_k and v_k denote the *process noise* and the *observation noise*, respectively (here assumed to be zero mean Gaussian noise with covariance matrices Q_k and R_k). Dynamic equations describe the dynamic behavior of the quadrotor in continuous-time, making easier to write the system as

$$\begin{aligned} \dot{x}(t) &= Ax(t) + Bu(t) + w(t) & ; & & w(t) &\sim \mathcal{N}(0, Q_c) \\ z(t) &= Cx(t) + v(t) & ; & & v(t) &\sim \mathcal{N}(0, R_c) \end{aligned}$$

where A and B are matrices that relate both state vector ($x(t)$) and control vector ($u(t)$) to the way the state vector varies over time ($\dot{x}(t)$). Solving the differential equation above and expressing them in discrete-time leads to

$$\begin{aligned} x_k &= e^{A\Delta t} x_{k-1} + e^{A\Delta t} \int_0^{\Delta t} e^{-A\tau} d\tau B u_{k-1} + w_k & ; & & w_k &\sim \mathcal{N}(0, Q_c \Delta t) \\ z_k &= C x_k + v_k & ; & & v_k &\sim \mathcal{N}(0, \frac{R_c}{\Delta t}) \end{aligned}$$

where Δt is the discretization step size, τ is the variable of integration from time 0 to time Δt , $e^{A\Delta t}$ is the state transition model F_k , $e^{A\Delta t} \int_0^{\Delta t} e^{-A\tau} d\tau B$ the control input model B_k and C is equal to the observation model H_k .

Conceptually, the algorithm works in a two-step process, i.e. a prediction and an update step. The prediction step uses the state estimate from the previous time step ($\hat{x}_{k-1|k-1}$) to produce an estimate of the state at the current time step ($\hat{x}_{k|k-1}$). Since this predicted step does not include observation information from the current time step it is also called the “*a priori* state estimate”. In the update step, the Kalman filter averages the “*a priori* prediction” with current observation information in order to refine the state estimate and generate an “*a posteriori* state estimate” ($\hat{x}_{k|k}$). This is done by using a weighted average, represented by the Kalman filter *gain* (K_k). The weights are calculated from the measurement noise covariance matrix R_k and the process noise covariance matrix Q_k in such a way that the values with smaller uncertainty have a

bigger weight within the estimation algorithm. The equations for the prediction and the update steps in discrete-time are the following

Prediction:

$$\hat{x}_{k|k-1} = F_k \hat{x}_{k-1|k-1} + B_{k-1} u_{k-1} \quad (\text{Predicted a priori state estimate})$$

$$P_{k|k-1} = F_k P_{k-1|k-1} F_k^T + Q_k \quad (\text{Predicted a priori estimate covariance})$$

Update:

$$K_k = \frac{P_{k|k-1} H_k^T}{H_k P_{k|k-1} H_k^T + R_k} \quad (\text{Optimal Kalman filter gain})$$

$$\hat{x}_{k|k} = \hat{x}_{k|k-1} + K_k (z_k - H_k \hat{x}_{k|k-1}) \quad (\text{Updated a posteriori state estimate})$$

$$P_{k|k} = P_{k|k-1} (I - K_k H_k) \quad (\text{Updated a posteriori estimate covariance})$$

where, for instance, $\hat{x}_{k|k-1}$ is read as the estimation of the state vector for instant k , done after receiving the measurement at the previous instant $k - 1$.

When the system model is non-linear, the Extended Kalman Filter (EKF) is used instead of the LKF. An example of its applicability on quadrotor attitude estimation is shown in [33]. The following figure shows the performance of a LKF for attitude estimation. It can be seen how gyroscopes and accelerometers in "stand alone" configuration are sensitive to drift and vibrations, respectively.

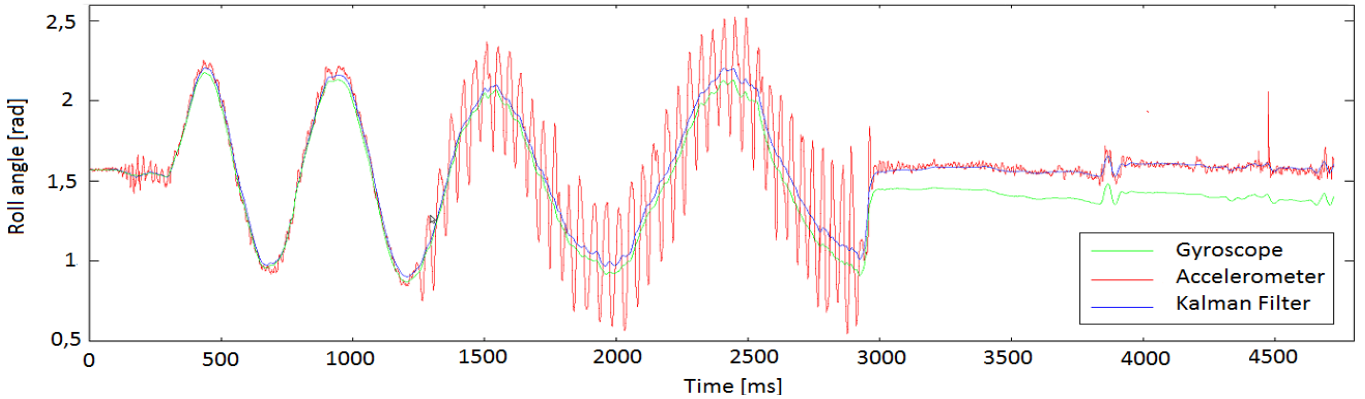


Figure 11: Roll angle estimation by solely using gyroscopes, accelerometers or LKF data fusion

3.2.2.2. Complementary filter (CF)

A complementary filter for attitude estimation performs low-pass filtering on a low-frequency attitude estimate, obtained from accelerometer data, and high-pass filtering on a biased high-frequency attitude estimate, obtained by direct integration of gyroscope output and fuses these estimates together to obtain an all-pass estimate attitude. The following diagram shows a simplification of how a linear CF works

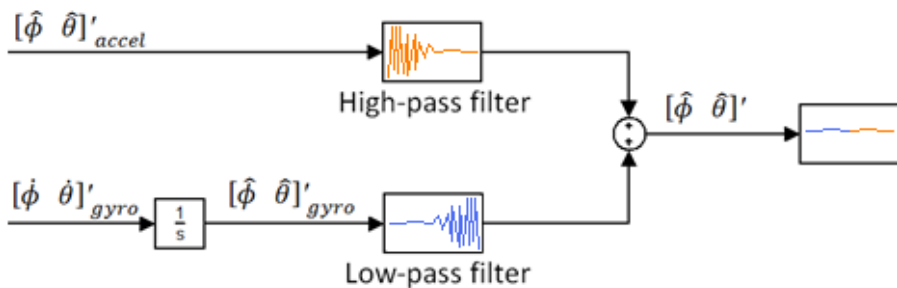


Figure 12: Operating principle of a Linear Complementary Filter for attitude estimation

Similarly, a CF for linear position and velocity estimation can be build using the GPS signal

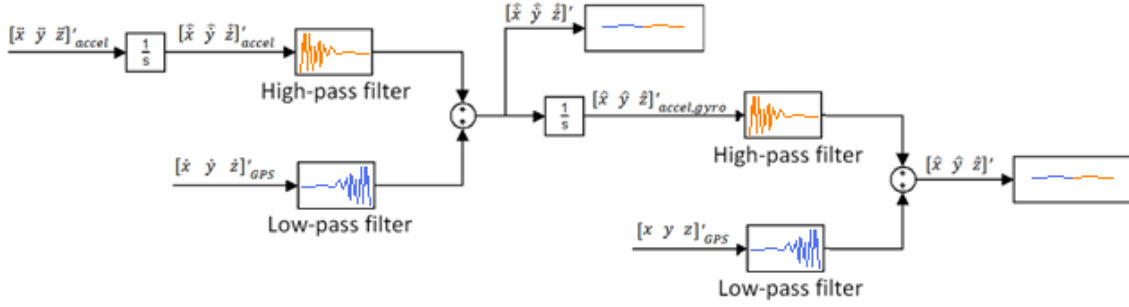


Figure 13: Operating principle of a Linear Complementary filter for linear position and velocity estimation

When a low pass estimate of the full attitude can be reconstructed from accelerometers, gyroscopes and magnetometers a non-linear CF can be used [34]. The idea behind the non-linear complementary filter for attitude estimation is to continuously update the rotation matrix R that defines the orientation of the UAV relative to the inertial frame of reference to keep its orthogonality. The numerical integration of the gyroscopes output, used as the primary source of attitude information, introduces numerical errors that slowly make the rotation matrix drift away from orthogonality, meaning that the length of the vectors represented by the matrix are not equal in the body frame and the inertial frame of reference. This leads into wrong results when computing the Euler angles in the inertial frame of reference. The following steps describe how to renormalize the rotation matrix [35]:

Given the rotation matrix $R = \begin{pmatrix} R_{xx} & R_{xy} & R_{xz} \\ R_{yx} & R_{yy} & R_{yz} \\ R_{zx} & R_{zy} & R_{zz} \end{pmatrix}$

- First, the dot product of the first two rows are computed. Since the result is supposed to be zero for an orthogonal matrix, this operation will give the error (or how much are they rotating toward each other).

$$Error = (R_{xx} \ R_{xy} \ R_{xz}) \cdot (R_{yx} \ R_{yy} \ R_{yz}) = (R_{xx} \ R_{xy} \ R_{xz}) \begin{pmatrix} R_{yx} \\ R_{yy} \\ R_{yz} \end{pmatrix}$$

- Second, half of the error is assigned each to the first and second row of R . The first two rows are then rotated in the opposite direction and the third row is forced to be orthogonal to the others by computing their cross product

$$(R_{xx} \ R_{xy} \ R_{xz})_{orthogonal} = (R_{xx} \ R_{xy} \ R_{xz}) - \frac{Error}{2} (R_{yx} \ R_{yy} \ R_{yz})$$

$$(R_{yx} \ R_{yy} \ R_{yz})_{orthogonal} = (R_{yx} \ R_{yy} \ R_{yz}) - \frac{Error}{2} (R_{xx} \ R_{xy} \ R_{xz})$$

$$(R_{zx} \ R_{zy} \ R_{zz})_{orthogonal} = (R_{xx} \ R_{xy} \ R_{xz})_{orthogonal} \times (R_{yx} \ R_{yy} \ R_{yz})_{orthogonal}$$

- Finally, the new rotation matrix $R_{orthogonal}$ is normalized by dividing each element of the matrix by the square root of the sums of the squares of the elements in its row. This normalized orthogonal rotation matrix is used in the next time step and then the update process is repeated.

3.2.3. Alternative methods

Motor power consumption: It is possible to estimate the Euler angles by relating voltage and current drawn from the motors to rotor thrust and, subsequently, to attitude. By applying both Kirchhoff and second Newton's law to a DC motor, its dynamic behavior can be described, relating both current and voltage consumption to rotational speed of the rotors. It turns out that rotor torque and thrust can be computed if rotational speed and two additional coefficients (which depend on the propeller geometry) are known. Lastly, once that thrust and torque of each rotor is known, estimation of the Euler angles can be done by applying the linear equations that describe the dynamic behavior of the vehicle. These equations for both the DC motor and the vehicle can be found in Section 4.1.1.1. and 4.1.1.3., respectively.

Last, this information could also be combined together with the other measurements as an additional observation within an attitude estimation algorithm such as the Kalman Filter.

3.3. Selecting the platform

This project tries to prove the feasibility of the use of a quadrotor as a wind measurement device itself. The goal is not to develop the platform from the beginning but to choose an existing platform and modify it if necessary.

3.3.1. Selection criteria

The chosen platform must satisfy the following requirements:

- **Open source Hardware:** The addition of extra sensors such as Pitot tubes may be desirable, as well as the fact of being able to modify hardware characteristics like endurance, maximum power, sensor accuracy, airframe and others. For this reason, the platform must allow the use of foreign parts.
- **Free software license:** Source code must be accessible and modifications allowed. For that, the platform has to have been developed under a free software license such as GPL.
- **Altitude hold:** Since it is necessary to keep the position in space while measuring, it is desirable that the platform is able to perform a flight while keeping a fixed altitude.
- **Waypoint navigation:** This feature allows the operator to simply set in the GCS the space coordinates of the desired measurement point. The quadrotor would carry out the mission automatically.

- **GCS:** A well organized Ground Control Station is desirable. Tuning of the control parameters can be done. In addition, real-time flight information can be displayed through a wireless telemetry system.
- **Flight time:** The platform should be capable of withstanding wind speeds up to 10 m/s for at least 10 minutes (considered in *Section 3.4.3*).
- **Wide online support:** It is convenient that the chosen platform has a wide online support, considering that some of the technical problems encountered may have been already solved by the online community.
- **Cost:** The selected platform should not exceed a maximum of 2000 €, RC transmitter, batteries and battery charger included.
- **Availability:** Last but not least, the platform has to be commercially available by the time this project is written. Shipping time is also considered.

Several Open Source Projects have been found that, to a greater or lesser degree, satisfy most or all the requirements mentioned above. Among them, the following 4 platforms have been studied: **Arducopter**, **MikroKopter**, **AeroQuad** and **OpenPilot**.

3.3.2. Platforms comparison [33]

- *ArduCopter*

Arducopter is a quadrotor autopilot project based on the Arduino framework. It has been developed by individual engineers worldwide and has one of the widest online communities associated to small rotorcrafts hobbyists. They offer fully assembled quadrotors with some customizable options such as GPS, sonar sensor and telemetry kit, and it uses an open-source license for both software and hardware designs.

- *AeroQuad*

AeroQuad is an open-source hardware and software project dedicated to the construction of quadrotors. As ArduCopter, it is also based on the Arduino platform. Almost-ready-to-fly quadrotors are available for purchase from the online store, although it is not as customizable as other quadrotor OSP.

- *MikroKopter*

MikroKopter is a small rotorcraft autopilot system developed in 2006 by a subsidiary of HiSystems GmbH. The platform's online community is well organized and suppliers can be found within Europe. It has already been used by researches, in most of the cases as an aerial high definition filming and shooting system, since its relative high payload capacity allows the user to equip the platform with a HD professional camera (only for 6- and 8-rotors configurations). Almost-ready-to-fly quadrotors are available for purchase.

- *OpenPilot*

OpenPilot is an Open Source UAV autopilot, designed by its online community, whose goal is making the platform especially suitable for aerial photography and aerial

videos applications. The system is still under strong development and no ready-to-fly quadrotors can be purchased at the moment.

The tables below resume the characteristics of each platform as well as the technical characteristics of the sensors on board:

Table 5: Platform comparison, according to the selection criteria [33]

	PLATFORM			
	<i>Arducopter</i>	<i>Mikrokopter</i>	<i>Aeroquad</i>	<i>Openpilot^a</i>
Processor	ATMega2560	ATMega644	Arduino ^b	STM32F103CB
OSP	YES	YES	YES	YES
License	LGPL	Proprietary License	GPL	GPL
GCS	YES	YES	YES	YES
RTF	YES	ARF ^c	ARF ^c	NO
Price (quadrotor)	~500 €	~1100 €	~400 €	-
Availability	YES	YES	YES	NO
Attitude estimation algorithm	NCF	LCF	NCF	EKF
Controller configuration	PI + P	PI	PID	PI + PI
GPS-based waypoint navigation	YES	YES	NO	NO
Altitude hold	YES	YES	YES	^c (Partially supported)
Client support	Blogs / Forums / Wiki	Blogs / Forum / Wiki	Blogs / Forums / Wiki	Forums / e-mail
Default sensors	3-axis Gyroscope <i>MPU6000</i> 3-axis Accelerometer <i>MPU6000</i> 3-axis Magnetometer <i>HMC5883L</i> GPS <i>uBlox-LEA-6H</i> Barometer <i>MS5611</i>	3x1-axis Gyroscope <i>ADXRS610</i> 3x1-axis Accelerometers <i>LIS344ALH</i> 3x1-axis Magnetometer <i>KMZ51</i> GPS <i>uBlox-LEA-6S</i> Barometer <i>BMP085</i>	3-axis Gyroscope <i>ITG3200</i> 3-axis Accelerometer <i>ADXL345</i> 3-axis Magnetometer <i>HMC5883L</i> GPS <i>uBlox_LEA-5</i> Barometer <i>BMP085</i>	1-axis Gyroscope <i>ISZ-500</i> 2-axis Gyroscope <i>IDC-500</i> 3-axis Accelerometer <i>ADX330</i> 3-axis Magnetometer <i>HMC5843</i> GPS <i>MT3329</i> Barometer <i>BMP085</i>
Additional sensors	Sonar Pitot tube Optical Flow sensor			Pitot tube

^a OpenPilot released a navigation system based on the MPU6000 while this project was being written.

^b The actual processor varies.

^c Board and structure have to be assembled.

Table 6: Gyroscope technical characteristics [36] [37] [38] [39] [40]

	<i>GYROSCOPES</i>			
	MPU-6000	IDG500 / ISZ500	ADXRS610	ITG3200
Technology	Digital	Analog	Analog	Digital
N° axis	3	2 / 1	1	3
ADC	16	^a	^a	16
Full Scale Range	X-/Y-/Z- Out Pins: ±250 °/s ±500 °/s ±1000 °/s ±2000 °/s	X-/Y-/Z- Out Pins: ±110 °/s ±500 °/s	Z- Output Pin: ±300 °/s	X-/Y-/Z- Out Pins: ±2000 °/s
Sensitivity	X-/Y-/Z- Out Pins: 131 LSB/(°/s) 65.5 LSB/(°/s) 32.8 LSB/(°/s) 16.4 LSB/(°/s)	X-/Y-/Z- Out Pins: 9.1 mV/(°/s) 2mV/(°/s)	Z- Output Pin: 6 mV/(°/s)	X-/Y-/Z- Out Pins: 14.375 LSB/(°/s)
ZRO	±20 °/s	1.35 V	2.5 V	±40 °/s
ODR	4 - 8000 Hz	-	-	4 - 8000 Hz
Power Supply Voltage	2.375 - 3.46 V	2.7 - 3.3 V	4.75 - 5.25 V	2.1 - 3.6 V

^a Requires external multiplexer

Table 7: Magnetometer technical characteristics[41][42][43]

	<i>MAGNETOMETERS</i>		
	HMC5883L	HMC5843	KMZ51
Technology	Digital	Digital	Analog
N° axis	3	3	1
ADC	12	12	^x
Full Scale Range	±8 gauss	±4 gauss	±2.5 gauss
Sensitivity	230/1370 LSB/gauss	512 LSB/gauss	6.4 mV/gauss
ZRO	±1.6 gauss	±0.55 gauss	±1.2 gauss
ODR	160 Hz	116 Hz	-
Power Supply Voltage	2.16 - 3.6 V	2.5 - 3.3 V	5 - 8 V

Table 8: Barometer technical characteristics [44][45][46]

	<i>BAROMETERS</i>		
	MS5611	MPX4115A0	BMP085
Technology	Digital	Analog	Digital
Full Scale Range	450 - 1100 hPa	150 - 1150 hPa	300 - 1100 hPa
Power Supply Voltage	1.8 - 3.6 V	4.85 - 5.35 V	1.8 - 3.6 V

Table 9: Accelerometer technical characteristics [47][48][49][50]

	ACCELEROMETERS				
	MPU-6000	ADXL330	ADXL345	BMA180	LIS344ALH
Technology	Digital	Analog	Digital	Digital	Analog
N° axis	3	3	3	3	3
ADC	16	^a	10 - 13	12 / 14	^a
Full Scale Range	X-/Y-/Z- Out Pins: ±2 g ±4 g ±8 g ±16 g	X-/Y-/Z- Out Pins: ±3.6 g	X-/Y-/Z- Out Pins: ±2 g ±4 g ±8 g ±16 g	X-/Y-/Z- Out Pins: ±1 g ±1.5 g ±2 g ±3 g ±4 g ±8 g ±16 g	X-/Y-/Z- Out Pins: ±2 g ±2.6 g
Sensitivity	X-/Y-/Z- Out Pins: 16384 LSB/g 8192 LSB/g 4096 LSB/g 2048 LSB/g	X-/Y-/Z- Out Pin: 300 mV/g	X-/Y-/Z- Out Pins: 256 LSB/g 128 LSB/g 64 LSB/g 32 LSB/g	Z- Output Pin: 8192 LSB/g 5460 LSB/g 4096 LSB/g 2730 LSB/g 2048 LSB/g 1024 LSB/g 512 LSB/g	X-/Y-/Z- Out Pin: 660 mV/g 220 mV/g
ZRO	±50 mg	1.2 - 1.8 V	±150 mg	±15 mg	1.2 - 1.8 V
ODR	4 - 1000 Hz	-	0.1 - 3200 Hz	1200 - 2400 Hz	-
Power Supply Voltage	2.375 - 3.46 V	1.8 - 3.6 V	2 - 3.6 V	2 - 3.6 V	2.4 - 3.6 V

^a Require external multiplexer.

3.3.3. Selection

The platforms studied are considered open source projects. However, only 3 of them (Arducopter, OpenPilot and AeroQuad) make use of a general public license (GPL). MikroKopter was released under a commercial proprietary license and thus, its software is allowed to be used only with the Licensor's products, preventing the use of the source code in other systems or with third party hardware [51].

Regarding attitude estimation, Openpilot implements the most efficient algorithm, the extended Kalman filter (EKF). Following in complexity are the Arducopter and the Aeroquad platform, both implementing the non-linear complementary filter (NCF), while MikroKopter uses a linear complementary filter (LCF). The control structures of each platform are described in [33]. When it comes to chips characteristics the MPU6000, used by Arducopter, has the best dynamic range among the accelerometers and gyroscopes described. Furthermore, it comes with a 9-

axis MotionFusion algorithm, able to access an external 3-axis magnetometer to gather a full set of sensor data without intervention from the system processor.

As far as waypoint navigation is concerned, only Arducopter and MikroKopter support this feature by default. When using the Satellite Based Augmentation System (SBAS), both uBlox-LEA-6H and uBlox-LEA-6S chips reach an accuracy of 2 m CEP (circular error probability) and 3 m of vertical accuracy. Nevertheless, the uBlox-LEA-6H chip on board the Arducopter supports the use of the European Galileo GNSS, which will offer accuracy an order of magnitude better than the other global navigations systems, giving it an advantage over the MikroKopter platform for near future projects (it is planned that the Galileo GNSS will be available by the year 2014).

Only the OpenPilot project does not support the *Altitude hold* feature without the addition of extra navigation electronics.

For the basic configuration, Arducopter and AeroQuad platforms offer the cheapest quadrotors, as opposed to MikroKopter which doubles the price. Arducopter RTF quadrotor can be purchased for less than 1100 € including a replacement kit with spare parts, radio control, sonar sensor and shipping costs from US to Germany, making it the better option concerning initial investment. Batteries and battery charger represent an extra cost below 200 €.

For the reasons previously stated, the selected platform is *ArduCopter*.

3.4. Flight time

As mentioned before, a reasonable flight time of 10 minutes under rough wind conditions is a requisite. The use of a battery and an electric cable are the options taken into account in order to power the UAV and to reach the desired flight time. The overall weight as a factor that limits the flight time is here considered as a topic itself.

3.4.1. Electric cable

The use of an electric cable to power the quadrotor from the ground through a conventional power source would eliminate the restriction of using batteries of any kind, saving money and time and, for practical purposes, making the flight time unlimited (nonetheless, stops every 30 minutes would be necessary to avoid overheating of the motors and damage). However, the altitude at which the quadrotor is intended to be flown makes one think that the weight of the cable will exceed the payload capacity of the vehicle at high altitudes.

According to the Arducopter site, the default motors can drain a current up to 27 A, meaning that, for a quadrotor configuration, the electric cable should be able to withstand a maximum of 108 A. After a succinct research considering copper and aluminum cables, it was found that its own weight would burden the quadrotor in excess, making it impossible to loiter beyond a few meters above ground and dismissing

this powering system. In case more powerful motors are used, cables could be an option. Higher altitudes could be reached and aerodynamic effects should be considered.

3.4.2. Battery

ArduCopter supports being powered by 3 cells and 4 cells LiPo batteries. When fully charged, a LiPo cell should be able to draw 4.2 V and when discharged it should never go below 3 V. The nominal voltage per cell is 3.7 V, meaning that if the battery rating is 3S (3 cells) it will draw an average of 11.1 V. The same way, if it is rated as 4S (4 cells) it will draw 14.8 V. A commercial LiPo battery with 4 cells weights ca. 30 % more than a 3 cells LiPo battery, per unit capacity. *Figure 14*, made compiling more than 50 commercial LiPo batteries, shows this fact. For this reason the battery choice will strongly affect the overall weight of the UAV, and thus, the flight time.

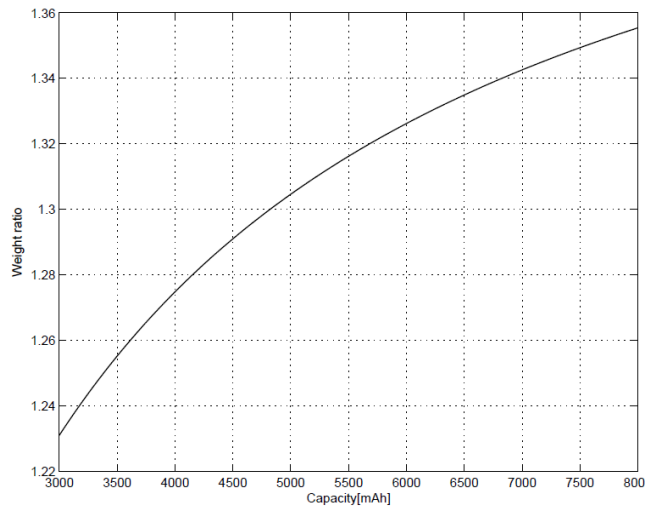


Figure 14: Weight ratio between 4 cells and 3 cells commercial LiPo batteries

3.4.3. Weight factor

Batteries are, by far, one of the components that burden the UAV the most. Consequently, a battery with a high energy storage/weight ratio is required. Among all the commercial batteries, the Lithium Polymer (LiPo) battery fulfills this requirement. A modern LiPo battery uses a gelled polymer electrolyte which decreases its internal resistance, enable the battery to deliver higher current burst. This feature allows small UAV such as quadrotors to keep a certain position while dealing with relatively strong wind gusts. In addition, LiPo batteries have the ability of being charged many times without losing capacity (generally up to 400 times), making them a better option over conventional rechargeable batteries such as Nickel-Cadmium (NiCad), Lithium-Ion (Li-Ion) or Nickel-Metal Hybrid (NiMH) batteries, and so popular among radio control hobbyist.

The weight of the UAV itself must also be considered. For long flight times a light platform is the best solution. The weight of a UAV basically depends on its size. Having the micro UAV with rotorcraft configuration in mind, it is obvious that a quadrotor will be lighter than a hexarotor and this at the same time lighter than an octorotor. The fewer the number of rotors, the lower the power consumption, and vice versa. On the other hand, the more the number of rotors, the higher the total thrust and thus, the bigger the battery the UAV is able to carry, increasing the flight time. Motors

and propellers must also be chosen carefully. The brushless motor can eventually burn out if the power draw from the battery exceeds the maximum power the motor can stand. Also, propellers could fall apart if they spin over the security limit suggested by the manufacturer.

For this project, brushless motors model AC2830-358, 850Kv are used, recommended for the Arducopter platform by their developers. These motors are able to withstand a maximum current of 27 A and to draw 200 W. The propeller suggested for this motor is a "Slow Flyer" APC-10x47, manufactured by Landing Products Inc. The angular velocity limit for "Slow Flyer" propellers is set by the manufacturer as a constant divided by the diameter of the propeller, measured in inches [52]. The limit for the chosen propeller is approximately 6500 rpm.

Finally, it must not be forgotten that, as a general rule, the overall performance of the UAV during a flight will get worse as its weight raises. The inertial effects will increase, making it harder for the UAV to face wind gusts with the sufficient celerity, even making it unstable. Given a particular UAV, the lightest configuration possible is preferred.

The following graphs ease the choice of the final configuration (hexarotors have been included to illustrate the dependency between number of rotors and flight time). *Figure 15* shows the relationship between battery weight (measured as battery capacity) and propeller angular velocity, for 4 and 3 cells LiPo batteries, and for 4- and 6-rotor configurations. Since the propellers are limited below 6500 rpm, the maximum capacity is automatically restricted. Propellers mounted on UAVs using 3 cells batteries spin slower than for those using 4 cells batteries. As pointed out before, 3 cells batteries are lighter than 4 cells batteries, making the UAV also lighter. This directly affects the required loitering thrust, decreasing it and the same time decreasing the propellers angular velocity. Also, it can be seen that propellers mounted on a hexarotor do not have to spin as fast as those mounted on the quadrotor. Even though a hexarotor is heavier than a quadrotor, the burden is shared by 6 rotors instead of 4, the loitering thrust produced by

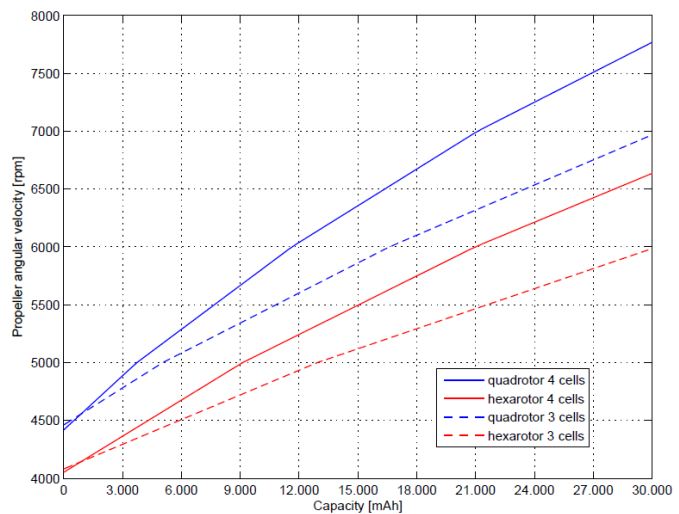


Figure 16: Propeller angular velocity vs. Battery capacity, comparing quadrotor and hexarotor for 3 and 4 cells LiPo batteries

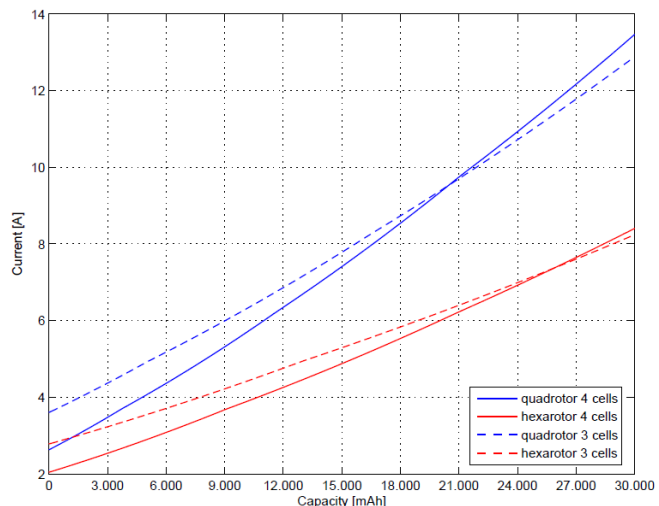


Figure 15: Current per motor vs. Battery capacity comparing quadrotor and hexarotor for 3 and 4 cells LiPo batteries

each motor drops and so it does the propeller angular velocity.

Given a minimum thrust and thus, given power consumption, UAVs motors using 3 cells batteries will drain a higher current than those using 4 cells batteries. However, it was shown that the propeller angular velocity increases with the battery capacity. As a matter of fact, propeller angular velocity increases at a higher rate for 4 cells batteries than for 3 cells batteries (*Figure 15*), clearing up why at some point the 4 cells battery UAV consume more current than the 3 cells battery UAV. Also, the minimum required thrust for a hexarotor is shared by 6 rotors instead of 4, consuming a quadrotor more current per motor than a hexarotor. Obviously, if current per motor is multiplied by number of rotors and quadrotor and hexarotor are compared, it is clear that hexarotors consume more current than quadrotors. This would make one think that a quadrotor could loiter for a longer time than a hexarotor, but this happens when both use the same battery capacity and below a reasonable battery capacity limit (*Figure 17*).

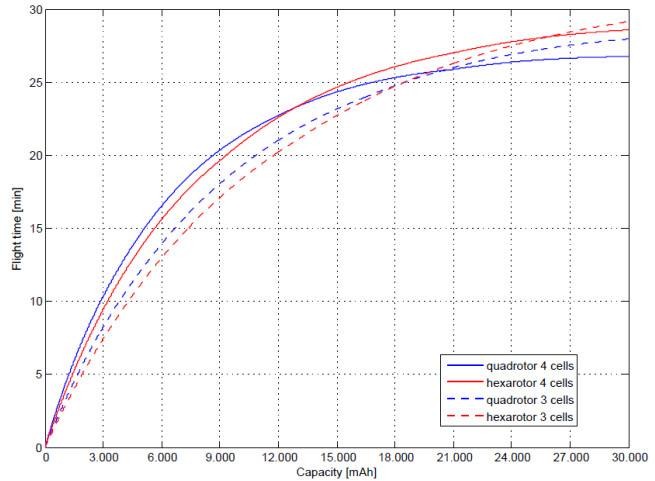


Figure 17: Flight time vs. Battery capacity, comparing Arducopter quadrotor and hexarotor for 3 and 4 cells LiPo

Nevertheless, it should be remember that a hexarotor is able to carry a heavier payload, such as a higher capacity battery, without exceeding neither the maximum rotational velocity of the propeller or the maximum power drained by the motor.

Figure 17 illustrates how quadrotors powered by 4 cells batteries are able to loiter for a longer time than those powered by 3 cells batteries. This is true for capacities below 20000 mAh. On the other hand, quadrotors stay in the air longer than hexarotors. This is true for low capacities, below 13000 mAh. Since the goal is to reach at least 10 minutes flight reducing weight at its maximum, the platform selected will be powered by a 6500 mAh LiPo battery, allowing a theoretic flight time of 15 minutes.

Chapter 4

Model

In this chapter a model of the platform is developed in Simulink®.

4.1. System model

As mentioned in *Section 3.1.2.*, a quadrotor needs a control algorithm in order to perform correctly. The system model was consequently divided into two major submodels, i.e. *Quadrotor model* and *Control model* (*Figure 18*). The wind vector as an input will go first through the *Quadrotor model*. It computes linear and rotational positions, velocities and accelerations of the quadrotor at a particular time, feeding some of these parameters to the *Control model*. Right after that, the *Control model* generates an output equivalent to the thrust that each motor should create in order to satisfy the conditions defined within the *Control model*. At the next time step, these thrusts feed the *Quadrotor model*, together with the next turbulent wind vector values, repeating the cycle.

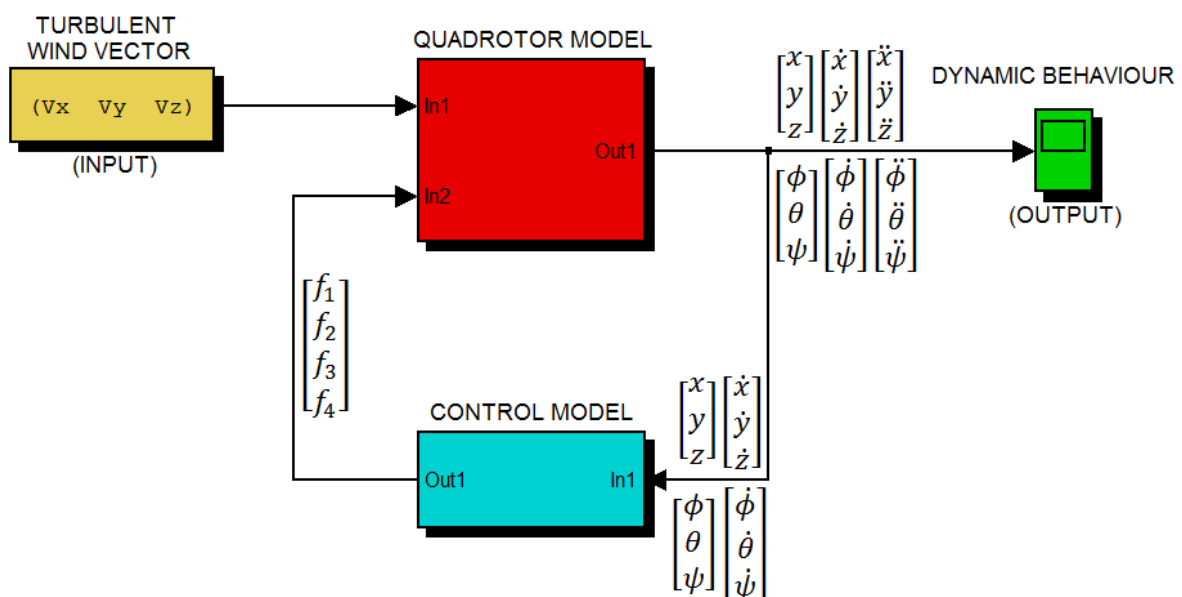


Figure 18: System model, divided into *Turbulent wind vector* as input, *Quadrotor model*, *Control model* and *Dynamic behavior* as output. Inputs and outputs are shown

At the same time, the *Quadrotor model* is divided into 3 submodels, i.e. *Aerodynamic model*, *Mechanical model* and *Motors model* (Figure 19)

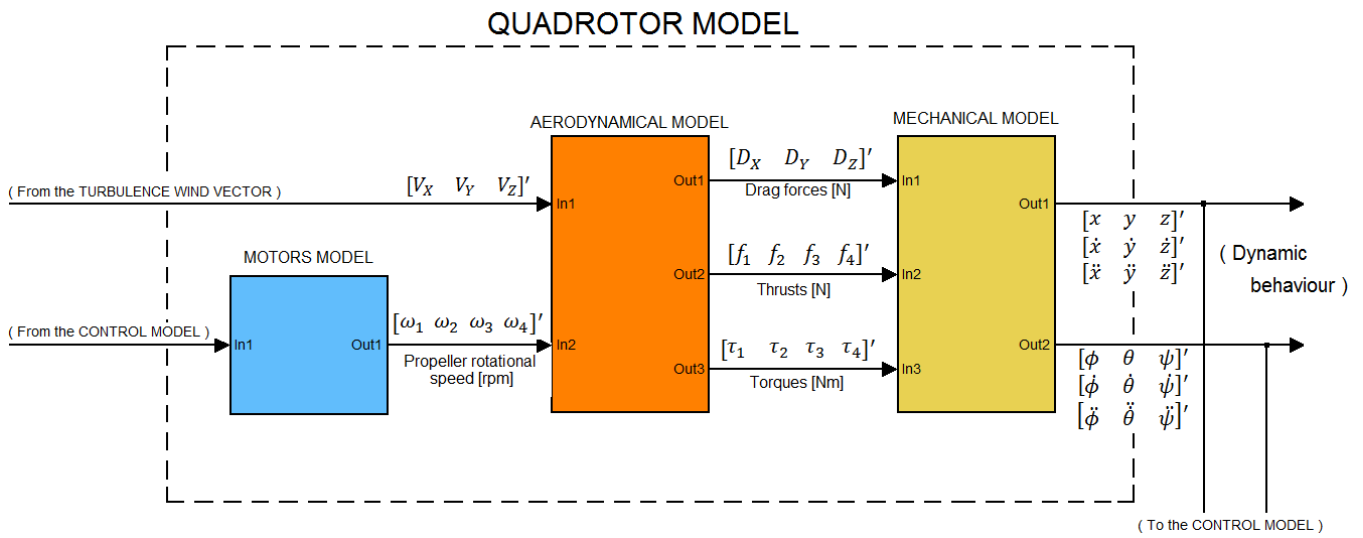


Figure 19: Quadrotor model, divided into *Motors model*, *Aerodynamical model* and *Mechanical model*

Similarly, the *Control model* is divided into 3 submodels, i.e. *PID Position control*, *PI Control* and *Thrust conversion* (Figure 20)

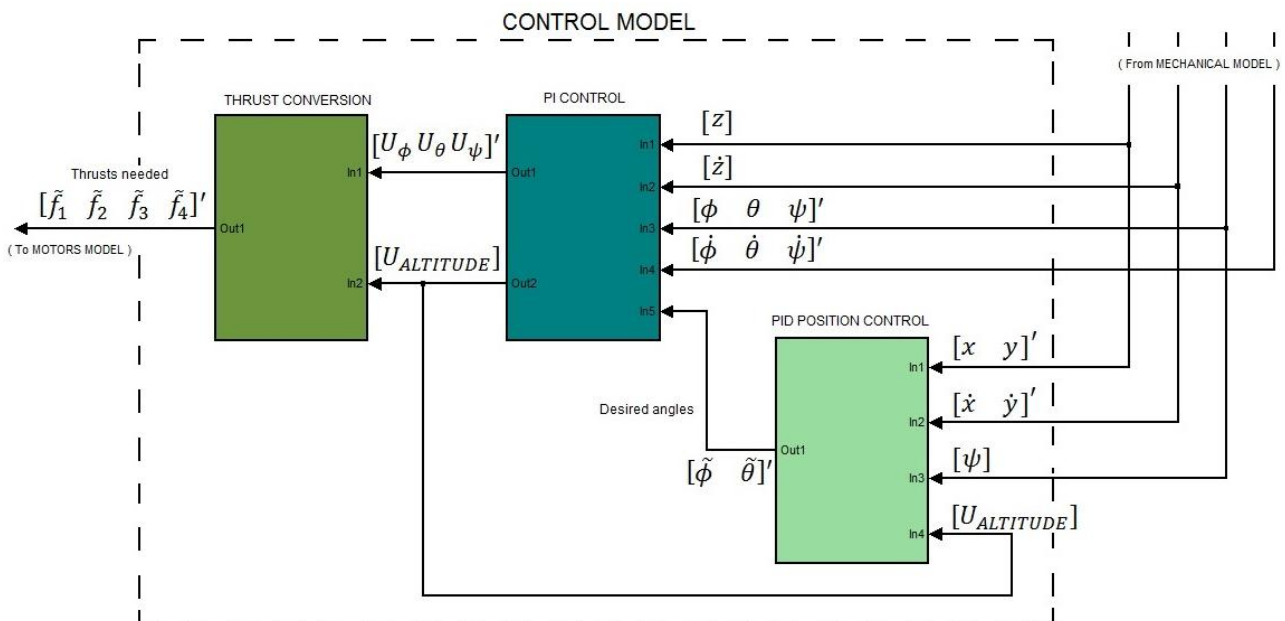


Figure 20: Control model, divided into *Thrust conversion*, *PI control* and *PID Position Control*

4.1.1. Quadrotor model

4.1.1.1. Motors model

It is common for small rotorcrafts to use brushless DC motors (BLDC) instead of brushed DC motors or glow engines. BLDC motors are equivalent to standard DC motors turned inside out, while the construction is similar to a multi-phase AC motor. Unlike DC motors, brushless motors' armature conductors rotate, while the magnetic field comprising the stator remains static. Since they have no brushes to reverse the polarity of the magnetic field, power transistors switching in synchronization with the rotor position perform it. This feature increases BLDC motors lifetime, making them more silent and efficient at converting electricity into mechanical power since there is no electrical or friction losses due to brushes. The only downside to the BLDC motors is its cost, slightly higher than DC motors. This difference arises mainly from the fact that they use a far more complex controller than the standard DC motors. The controller is commonly known as ESC (Electronic Speed Controller). This controller works in fact as a pulse-modulation controller (PWM), applying full voltage to the motor, turning it on and off rapidly. By varying the ratio of on-time to off-time, the speed control varies the average voltage that the motor sees.

Table 10 resumes the advantages of using a BLDC motor over DC motors or glow engines:

Table 10: Comparison between BLDC motors over Glow engines and standard DC motors

	Advantages over ...		Disadvantages
	Standard DC motors	Glow engines	
<i>BLDC motors</i>	More efficient		Require advance ESC
	Less noisy		
	Less maintenance		
	More reliable at high speeds	No polluting	Higher cost
	Longer lifetime	Less weight	

Since the performance of BLDC motors and standard DC motors are similar, a DC motor was modeled for the sake of simplicity [53]. After applying both Newton's and Kirchhoff law to the motor system, the following equations are obtained

$$J \frac{d^2\theta}{dt^2} = k_t i - \tau_{load} - B \frac{d\theta}{dt}$$

$$V = Ri + L \frac{di}{dt} + k_e \frac{d\theta}{dt}$$

where J denotes the rotor inertia in $[\text{Kgm}^2]$, θ the angular position of the rotor in $[\text{rad}]$, k_t the motor constant in $[\text{Nm/A}]$, i the current in $[\text{A}]$, τ_{load} the resistive torque in $[\text{Nm}]$, B the friction torque constant in $[\text{Nms}]$, V the voltage in $[\text{V}]$, R the terminal resistance in $[\Omega]$, L the terminal inductance in $[\text{H}]$ and k_e the back-emf constant in $[\text{Vs/rad}]$. The DC motor model results as follows:

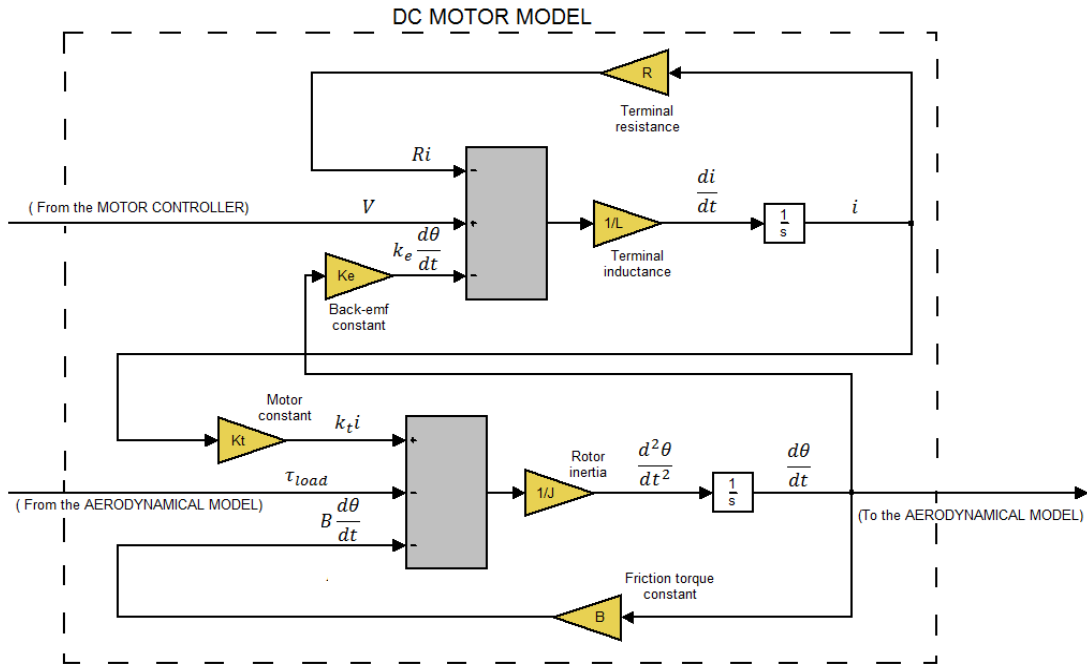


Figure 21: DC motor model

Technical data for the BLDC motor "AC2830-358, 850Kv" was not available. The following parameters have been either estimated or taken from a BLDC motor of similar performance (the Friction torque constant was assumed to be zero)

Table 11: Technical data for BLDC motor AC2830-358, 850 Kv

"AC2830-358, 850Kv"	
Resistance $[\Omega]$	0.2491
Inductance $[\text{H}]$	0.005
Motor constant $[\text{Nm/A}]$	$1123.45 \cdot 10^{-5}$
Friction torque constant $[\text{Nms}]$	0
Back-emf constant $[\text{Vs/rad}]$	$1123.45 \cdot 10^{-5}$
Inertia $[\text{Kgm}^2]$	$2.0834 \cdot 10^{-5}$

Since this model represents a standard DC motor and not a BLDC motor, the motor controller in the model can directly feed a voltage signal instead of pulses. To do so, the controller relates the input signal "thrust needed" coming from the *Control model* to the output signal "Voltage level" needed by the particular combination motor-propeller in order to generate such thrust. Once motor and propeller have been chosen, generated thrust can be related to voltage and to wind speed orthogonal to the propeller

plane V_{Bz} by means of a look-up table. The maximum voltage has been restricted to 14.8 V, which is the maximum voltage a 4 cells LiPo battery offers.

Voltage increases not only with thrust but also with V_{Bz} . If it is also taken into account that aerodynamic resistance increases with wind speed (and so does the power consumed), there are two reasons why power consumption of a rotor increases under windy conditions. It is worth mentioning that the increment of power consumption due to aerodynamic resistance is much higher than that caused by V_{Bz} .

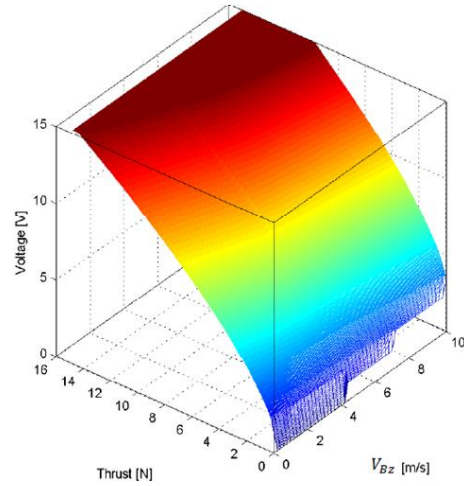


Figure 22: Relation between Thrust, wind speed orthogonal to the propeller plane and voltage

4.1.1.2. Aerodynamic model

The goal of this block is to provide values of thrusts, torques and drag forces to the *Mechanical model*, needed to apply the dynamic equations and thus, to find out the dynamic behavior of the quadrotor.

The model is divided into 3 small submodels:

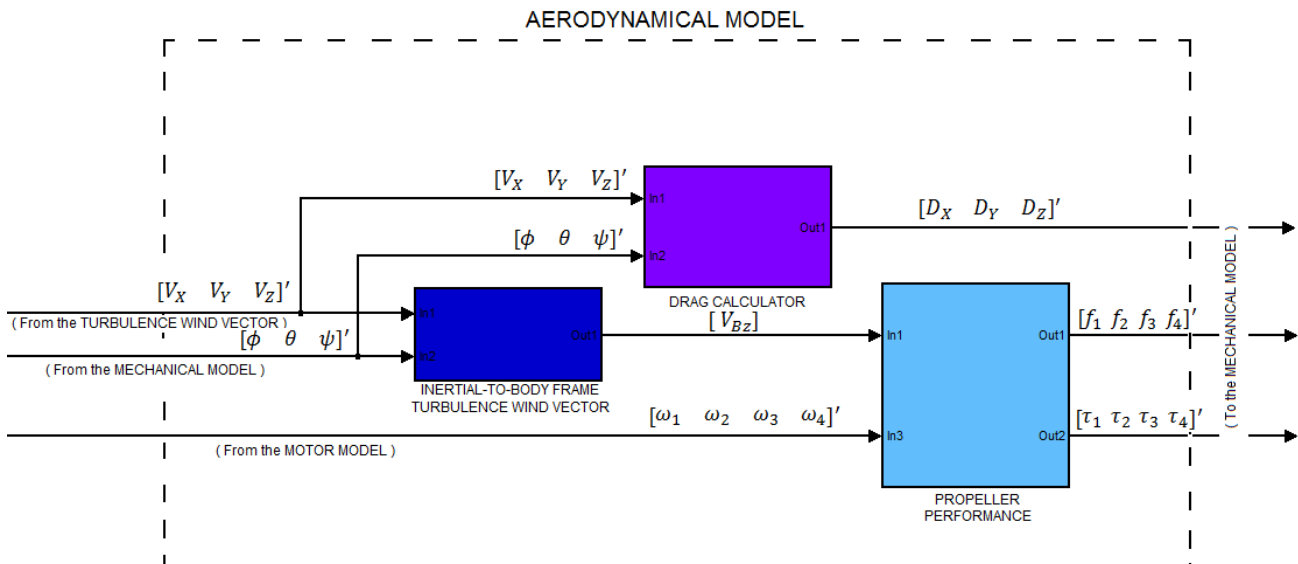


Figure 23: Aerodynamic model, divided into *Inertial-to-Body frame turbulence Wind Vector* model, *Drag Calculator* model and *Propeller Performance* model

The first submodel (*Inertial-to-Body frame turbulence wind vector*) transforms the turbulent wind vector from the inertial frame to the body frame. This is achieved by multiplying the turbulent wind vector by the rotation matrix transpose R^T . This has to be done because the *Propeller performance* model not only needs the value of the rotational velocity of the rotor in order to find the appropriate torques and thrusts, but also the value of V_{Bz} at each time step.

$$\begin{bmatrix} V_{Bx} \\ V_{By} \\ V_{Bz} \end{bmatrix} = R^T \begin{bmatrix} V_x \\ V_y \\ V_z \end{bmatrix}$$

The second submodel (**Drag Calculator**) computes the drag forced associated with the turbulent wind components using the dynamic pressure equation

$$\begin{bmatrix} D_x \\ D_y \\ D_z \end{bmatrix} = \frac{1}{2} \rho_{air} I \begin{bmatrix} A_x \\ A_y \\ A_z \end{bmatrix} \begin{bmatrix} V_x^2 & 0 & 0 \\ 0 & V_y^2 & 0 \\ 0 & 0 & V_z^2 \end{bmatrix} \begin{bmatrix} C_x \\ C_y \\ C_z \end{bmatrix}$$

where D is the drag force in the inertial frame in [N], ρ_{air} is the air density in [kg/m³], A is the area of the quadrotor exposed to the wind in [m²], V is the wind speed in [m/s] and C is the drag coefficient associated with the quadrotor profile. The main problem in this equation is to find the area exposed and the drag coefficient. As far as aerodynamic is concern, it is assumed that the quadrotor behaves as an angled cube. The drag coefficient is selected as 0.9, constant and equal for the three axis. The use of CAD software allows modeling the quadrotor and gives an idea about the order of magnitude of the minimum and maximum areas in [mm²]. Additionally, it is considered that the areas swept by the propellers have a big effect on the drag forces, behaving as semi-permeable disks that put up resistance against the turbulent wind. *Figure 24* shows the approximate area for tilt angles 0°, 30° and 45°.


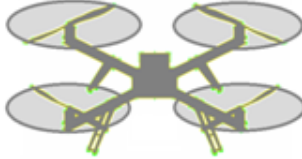
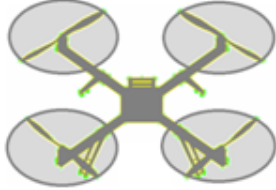
		
$Area_{0^\circ} \sim 270000 \text{ mm}^2$	$Area_{30^\circ} \sim 298000 \text{ mm}^2$	$Area_{45^\circ} \sim 308000 \text{ mm}^2$

Figure 24: Quadrotor area estimation

The equation that describes the relation between tilt angle and area exposed is:

$$A = (4P_s R^2 \pi \sin(\gamma) + A_o)$$

where A denotes the area exposed in [m²], P_s is the coefficient that expresses the semi-permeable nature of the rotating propeller, R is the radius of the propeller in [m], γ is the tilt angle in [°] (combination of pitch and roll angles) and A_o is the minimum area exposed in [m²], corresponding to zero pitch and zero roll angles.

The third submodel (*Propeller performance*) uses a look-up table to calculate the values of thrust and torque generated by each rotor. Thrust force and torque can be calculated by multiplying rotor rotational velocity squared ω_{Mi}^2 by a lift coefficient k and by a drag coefficient b , respectively. Although these coefficients vary, they can be calculated from the performance table provided by the propeller manufacturer. *Figure 25*, generated by the model, shows how the coefficient varies for a given rotor rotational

velocity (with the scale graduated as a thrust and as a torque scale, respectively) at different wind speed components orthogonal to the propeller plane V_{Bz} . Nevertheless, for low values of thrust and torque and maximum values of V_{Bz} around 1 m/s, k and b can be assumed to be constant, with values of $1.4 \cdot 10^{-5}$ [Ns²] and $3 \cdot 10^{-7}$ [Nms²] respectively (the model does not make this assumption).

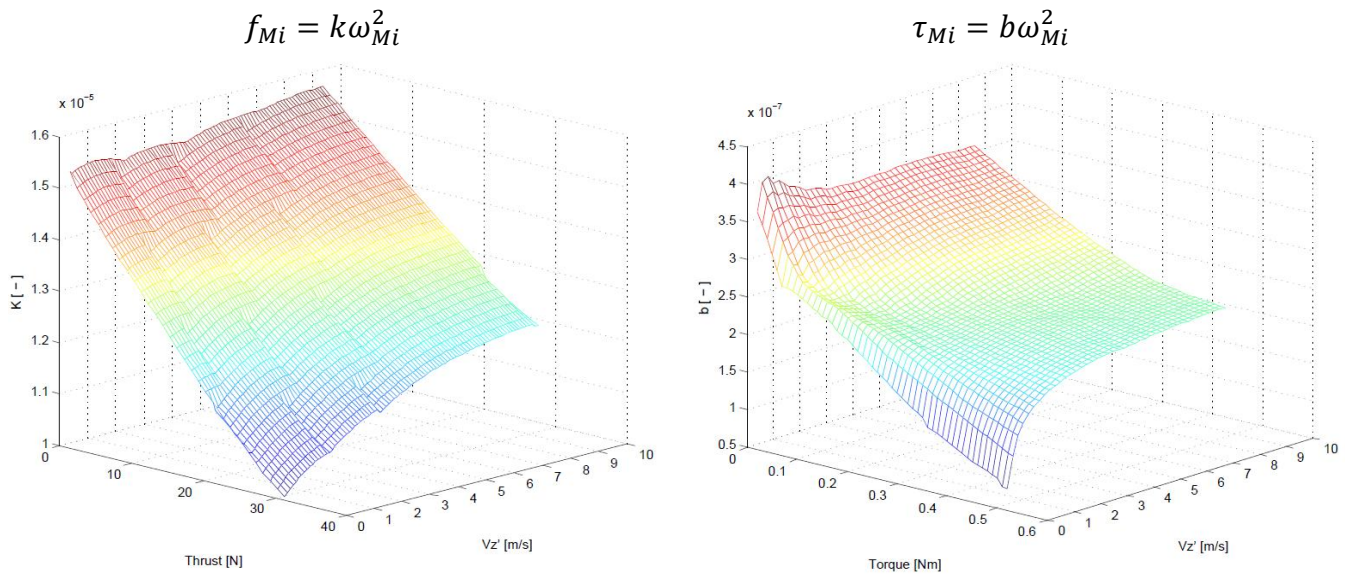


Figure 25: Coefficients k and b for the selected propeller, related to thrust, torque and wind speed components orthogonal to the propeller plane

4.1.1.3. Mechanical model [54]

The *Mechanical model* comprises the linear and rotational equations that describe the dynamic behavior of the quadrotor. These equations are derived from the Euler-Lagrange formalism assuming a symmetric, rigid body structure. It is divided into two submodels, i.e. *Linear Equations Model* and *Rotational Equations Model*.

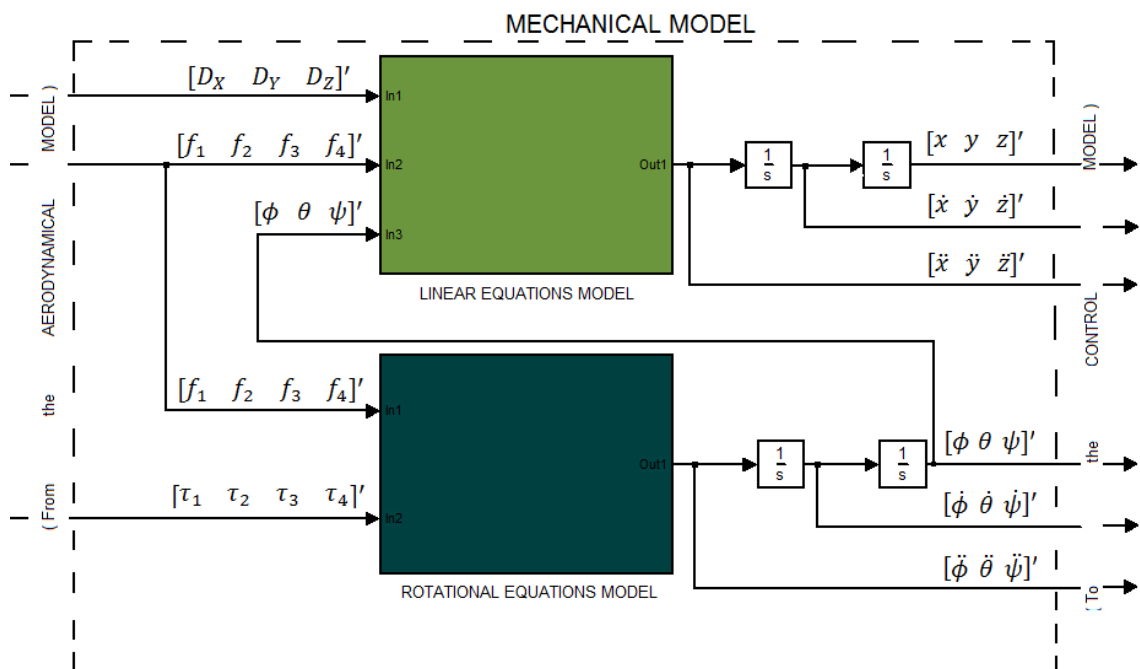


Figure 26: Mechanical model, divided into Linear Equations Model and Rotational Equations Model 48

Since the quadrotor is expected to fly within the range of a few hundred meters, only an inertial frame of reference and a body frame of reference are needed. The inertial frame of reference (x, y, z) is fixed to an arbitrary point on the Earth's surface, following the ENU coordinates convention (x - geodetic East, y - geodetic North, z - Up). The body frame of reference (x_B, y_B, z_B) is rigidly fixed to the center of gravity of the vehicle. Both reference systems are shown in *Figure 27*:

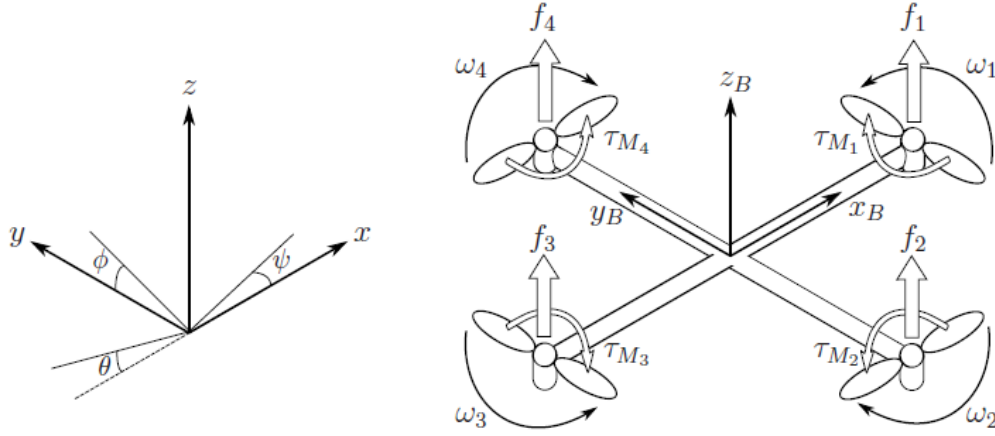


Figure 27: Inertial and Body frames of the quadrotor, Euler angles, thrusts and torques convention

Absolute position of the center of gravity is defined in the inertial frame with the vector ξ and attitude is defined in the inertial frame with three Euler angles η . Following the right-hand rule, roll, pitch and yaw angles are considered positive as rotations around the x -axis, y -axis and z -axis respectively.

$$\xi = \begin{bmatrix} x \\ y \\ z \end{bmatrix} \quad ; \quad \eta = \begin{bmatrix} \phi \\ \theta \\ \psi \end{bmatrix}$$

In the body frame the linear velocity vector $\dot{\xi}_B$ and the angular velocity vector $\dot{\eta}_B$ are defined as follows

$$\dot{\xi}_B = \begin{bmatrix} \dot{x} \\ \dot{y} \\ \dot{z} \end{bmatrix} \quad ; \quad \dot{\eta}_B = \begin{bmatrix} \dot{\phi} \\ \dot{\theta} \\ \dot{\psi} \end{bmatrix}$$

To transform angles from the body frame to the inertial frame the rotation matrix R is used. This matrix follows the right-hand rule and the rotation order convention $Z_\psi Y_\theta X_\phi$

$$R = \begin{pmatrix} C_\phi C_\theta & C_\phi S_\theta S_\phi - S_\phi C_\phi & C_\phi S_\theta C_\phi + S_\phi S_\phi \\ S_\phi C_\theta & S_\phi S_\theta S_\phi + C_\phi C_\phi & S_\phi S_\theta C_\phi - C_\phi S_\phi \\ -S_\theta & C_\theta S_\phi & C_\theta C_\phi \end{pmatrix}$$

where C denotes \cos and S denotes \sin .

Additionally, the rotation matrix W_η is defined, performing the transformation of angular velocities from the inertial frame to the body frame:

$$W_\eta = \begin{pmatrix} 1 & 0 & -S_\theta \\ 0 & C_\theta & C_\theta S_\theta \\ 0 & -S_\theta & C_\theta C_\theta \end{pmatrix}$$

Similarly, the inverse of W_η will perform the opposite transformation, i.e. from the body frame to the inertial frame. It is assumed that $\theta \neq \frac{(2k-1)\pi}{2}, (k \in \mathbb{Z})$

$$W_\eta^{-1} = \begin{pmatrix} 1 & S_\theta T_\theta & C_\theta T_\theta \\ 0 & C_\theta & -S_\theta \\ 0 & S_\theta/C_\theta & C_\theta/C_\theta \end{pmatrix}$$

where T denotes \tan .

As a consequence of the symmetric structure assumption, the inertia matrix I is diagonal. Additionally, the arms of the quadrotor are aligned with the x and y-axis on the body frame, making I_{xx} and I_{yy} equal.

$$I = \begin{pmatrix} I_{xx} & 0 & 0 \\ 0 & I_{xx} & 0 \\ 0 & 0 & I_{zz} \end{pmatrix}$$

As mentioned in *Section 4.1.1.3.*, dedicated to the *Mechanical model*, thrust f_{Mi} can be ideally expressed as the product of a coefficient k and the rotor rotational velocity squared ω_{Mi}^2

$$f_{Mi} = k\omega_{Mi}^2$$

and torque τ_{Mi} as the product of a coefficient b and the rotor rotational velocity squared ω_{Mi}^2 . An additional term involving rotor inertia moment I_M and its angular acceleration $\dot{\omega}_{Mi}$ should be added to the equation (this term was already considered in the motor model). The complete equations is

$$\tau_{Mi} = b\omega_i^2 + I_M\dot{\omega}_{Mi}$$

Total thrust T is aligned with the z- axis on the body frame, and it is simply the sum of the 4 thrusts generated by the rotors

$$T = \sum_{i=1}^4 f_{Mi}$$

Torques around z-, y- and x- axis are respectively defined as τ_ψ , τ_ϕ and τ_θ

$$\begin{bmatrix} \tau_\phi \\ \tau_\theta \\ \tau_\psi \end{bmatrix} = \begin{bmatrix} l(-f_{M2} + f_{M4}) \\ l(-f_{M1} + f_{M3}) \\ \sum_{i=1}^4 \tau_{Mi} \end{bmatrix}$$

where l denotes the distance in [m] between the origin of the body frame and the rotor.

The Lagrangian \mathcal{L} is the difference between kinetic energy and potential energy

$$\mathcal{L} = E_{\text{kin}} - E_{\text{pot}} = (E_{\text{trans}} + E_{\text{rot}}) - E_{\text{pot}} = \frac{1}{2}m\dot{\xi}^2 + \frac{1}{2}I\dot{\eta}_B^2 - mgz$$

The jacobian matrix J is now defined

$$J = W_\eta^T I W_\eta$$

Studying the lineal and rotational components of \mathcal{L} separately yields to the final equations that described the dynamic behavior of the quadrotor

$$\begin{aligned} \ddot{\xi} &= \begin{pmatrix} \ddot{x} \\ \ddot{y} \\ \ddot{z} \end{pmatrix} = -g \begin{pmatrix} 0 \\ 0 \\ 1 \end{pmatrix} + \frac{1}{m} R \begin{pmatrix} 0 \\ 0 \\ T \end{pmatrix} - \frac{1}{m} \begin{pmatrix} D_x \\ D_y \\ D_z \end{pmatrix} \\ \ddot{\eta} &= \begin{pmatrix} \ddot{\phi} \\ \ddot{\theta} \\ \ddot{\psi} \end{pmatrix} = J^{-1} \left(\begin{pmatrix} \tau_\phi \\ \tau_\theta \\ \tau_\psi \end{pmatrix} - C \begin{pmatrix} \dot{\phi} \\ \dot{\theta} \\ \dot{\psi} \end{pmatrix} \right) \end{aligned}$$

where $\ddot{\xi}$ denotes the linear accelerations in the inertial frame in [m/s²], $\ddot{\eta}$ the rotational accelerations in the inertial frame in [rad/s²] and $C = f(I, \eta, \dot{\eta})$ is the Coriolis term, containing the gyroscopic and centripetal terms.

After representing these equations in Matlab/Simulink® it is possible to get the linear $\ddot{\xi}$ and rotational $\ddot{\eta}$ accelerations of the quadrotor. By integrating these values, linear and rotational velocities $\dot{\xi}$, $\dot{\eta}$ and positions ξ , η are also obtained.

4.1.2. Control model [15]

The control model is divided into 3 submodels, i.e. a *PID position control model*, a *PI control model* and a *Thrust conversion model*.

The goal of the first model (***PID Position Control***) is to compute the desired roll and pitch angles, which will be the future set-points for the PI control model. Since the goal of this project is to measure the wind speed at a certain position in space, it is necessary to control the quadrotor attitude to keep this position. In order to do so, horizontal displacement is fixed as a set-point. By comparing the set-points with the actual horizontal position and using a PID controller, it is possible to compute the attitude the quadrotor should adopt in order to maintain the desired position. The following equations are implemented in this block

$$\begin{bmatrix} \phi_d \\ \theta_d \end{bmatrix} = \frac{m}{U_z} \begin{bmatrix} -S_\psi & -C_\psi \\ C_\psi & -S_\psi \end{bmatrix}^{-1} \begin{bmatrix} \ddot{x}_d \\ \ddot{y}_d \end{bmatrix}$$

The goal of the second model (***PI control***) is to find the 4 control signals U_{roll} , U_{pitch} , U_{yaw} and U_{alt} which will be used to compute the needed thrust that each motor should generate in order to reach and keep the desired position. Strictly speaking the model represents a PI controller; however, the rate at which the attitude varies has been included in order to introduce a derivative dependence. The following equations are included within this model

$$\begin{aligned} U_{roll} &= K_P(K_{Pe}(\phi_d - \phi) - \dot{\phi}) + K_I \int_0^t (\phi_d - \phi) d\tau \\ U_{pitch} &= K_P(K_{Pe}(\theta_d - \theta) - \dot{\theta}) + K_I \int_0^t (\theta_d - \theta) d\tau \\ U_{roll} &= K_P(K_{Pe}(\psi_d - \psi) - \dot{\psi}) + K_I \int_0^t (\psi_d - \psi) d\tau \\ U_{alt} &= K_{Pz}(K_{Pze}(z_d - z) - \dot{z}) + K_{Iz} \int_0^t (z_d - z) d\tau \end{aligned}$$

where K_P , K_{Pe} , K_I and K_{Pz} , K_{Pze} , K_{Iz} are the proportional, stabilize and integral gains for the attitude and the altitude, respectively; t is the instantaneous time and τ denotes the variable of integration from time 0 to time t .

The third model (***Thrust conversion***) transforms the signals generated by the second model into thrusts in [N]. These are the thrusts that the rotors must generate in order to reach and keep the desired position. The following equations are implemented in this block

$$\begin{aligned} f_1 &= \frac{1}{4}U_{alt} - \frac{1}{2}U_{pitch} - \frac{1}{4}U_{yaw} \\ f_2 &= \frac{1}{4}U_{alt} - \frac{1}{2}U_{roll} + \frac{1}{4}U_{yaw} \\ f_3 &= \frac{1}{4}U_{alt} + \frac{1}{2}U_{pitch} - \frac{1}{4}U_{yaw} \\ f_4 &= \frac{1}{4}U_{alt} + \frac{1}{2}U_{roll} + \frac{1}{4}U_{yaw} \end{aligned}$$

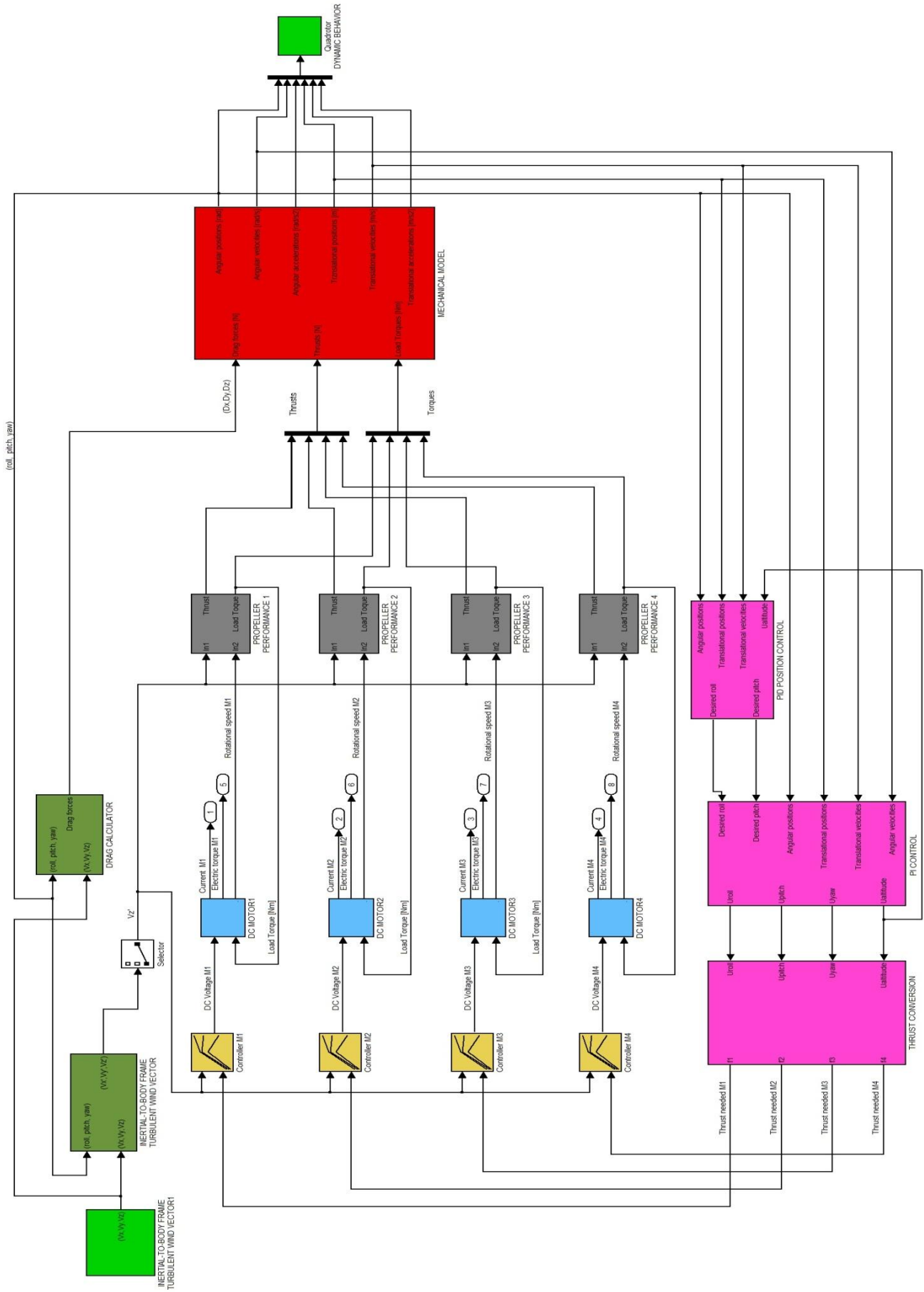


Figure 28: Model overview

Chapter 5

Wind speed calculation

5.1. Drag force calculation methods

As mentioned in *Section 2.3.*, three approaches have been followed in order to estimate the wind profile. This section attempts to give a deeper understanding concerning these approaches. In all cases, once the drag force has been calculated, equations derived in *Section 2.3.* are used to calculate wind speed and wind direction. As a result, this chapter attempts to explain the three methods considered to figure out the drag force acting against the quadrotor. Once the drag force is estimated, wind speed calculation is straightforward.

5.1.1. Simple method

This method does not take into account dynamic effects. It assumes the quadrotor to hover in a steady position, without changes in accelerations or velocities. The drag force acting on the quadrotor can be calculated from the tilt angle (γ) as follows

$$D_{simple} = mg \tan(\gamma)$$

where (γ) is computed with equation from *Section 2.3.* Wind can now be calculated.

5.1.2. Linear equation method

This method makes use of the dynamic linear equations derived in *Section 4.1.1.3.* to clear up the drag forces. The linear equation for each axis results in

$$\begin{aligned}\ddot{x} &= \frac{1}{m} [(C_\varphi S_\theta C_\phi + S_\varphi S_\phi)T - D_x] \\ \ddot{y} &= \frac{1}{m} [(S_\varphi S_\theta C_\phi - C_\varphi S_\phi)T - D_y]\end{aligned}$$

$$\ddot{z} = \frac{1}{m} [(C_\theta C_\phi)T - D_z] - g$$

Clearing up the drag forces gives

$$D_x = (C_\phi S_\theta C_\phi + S_\phi S_\theta)T - \dot{x}m$$

$$D_y = (S_\phi S_\theta C_\phi - C_\phi S_\theta)T - \dot{y}m$$

$$D_z = (C_\theta C_\phi)T - gm - \dot{z}m$$

Total thrust T could be calculated either through the rotational equations and the equation relating thrust and rotational wind speed of the rotor or estimated by using the third linear equation and disregarding the drag force D_z . The equations needed in the first case are

$$T = k(\omega_{M1}^2 + \omega_{M2}^2 + \omega_{M3}^2 + \omega_{M4}^2)$$

$$\tau_\phi = lk(\omega_{M4}^2 - \omega_{M2}^2)$$

$$\tau_\theta = lk(\omega_{M3}^2 + \omega_{M1}^2)$$

$$\tau_\psi = b(\omega_{M1}^2 + \omega_{M2}^2 + \omega_{M3}^2 + \omega_{M4}^2)$$

First and fourth equations are linearly dependent. With 4 unknown quantities ($\omega_{M1}^2, \omega_{M2}^2, \omega_{M3}^2$ and ω_{M4}^2) and only three equations at least one ω is needed. This variable could be either be measured directly with a dedicated sensor or calculated from the equations that describe the dynamic behavior of the motor. In order to do this, at least current and voltage have to be known, which is not the case (the *Arducopter* version used does not feature ammeter or voltmeter sensors). For this reason, T is calculated here disregarding D_z . The equation results in

$$T = \frac{(\ddot{z} + g)m}{C_\theta C_\phi}$$

Accelerations in the inertial frame of reference are obtained from the accelerometers. To convert raw data in the body frame into acceleration units in the inertial frame it is proceeded as follows

$$\begin{pmatrix} \ddot{x} \\ \ddot{y} \\ \ddot{z} \end{pmatrix} = R \begin{pmatrix} \ddot{x}_{RAWacc} \\ \ddot{y}_{RAWacc} \\ \ddot{z}_{RAWacc} \end{pmatrix} \frac{g}{1024} + \begin{pmatrix} 0 \\ 0 \\ g \end{pmatrix}$$

Substituting the last two expressions above in the drag force equations for the X- and Y-axis results in

$$D_x = (C_\varphi S_\theta C_\phi + S_\varphi S_\phi) \frac{\left(\{ [R_{31}\ddot{x}_{RAWacc} + R_{32}\dot{y}_{RAWacc} + R_{33}\ddot{z}_{RAWacc}] \frac{g}{1024} + g \} + g \right) m}{C_\theta C_\phi} - \{ [R_{11}\ddot{x}_{RAWacc} + R_{12}\dot{y}_{RAWacc} + R_{13}\ddot{z}_{RAWacc}] \frac{g}{1024} \} m$$

$$D_y = (S_\varphi S_\theta C_\phi - C_\varphi S_\phi) \frac{\left(\{ [R_{31}\ddot{x}_{RAWacc} + R_{32}\dot{y}_{RAWacc} + R_{33}\ddot{z}_{RAWacc}] \frac{g}{1024} + g \} + g \right) m}{C_\theta C_\phi} - \{ [R_{21}\ddot{x}_{RAWacc} + R_{22}\dot{y}_{RAWacc} + R_{23}\ddot{z}_{RAWacc}] \frac{g}{1024} \} m$$

where R_{ij} denotes the component in the i^{th} row and in the j^{th} column of R .

The drag force used as input in the wind speed calculation algorithm is the resultant from D_x and D_y

$$D_{l.eq} = \sqrt{D_x^2 + D_y^2}$$

Wind vector can now be calculated.

5.1.3. Kalman filter method

The third method for drag force estimation makes use of a Kalman filter. The model assumes the form in continuous time form

$$\underbrace{\begin{pmatrix} \ddot{x} \\ \dot{x} \\ \dot{D}_x \\ \ddot{y} \\ \dot{y} \\ \dot{D}_y \\ \ddot{z} \\ \dot{z} \\ \dot{D}_z \end{pmatrix}}_{\dot{y}} = A \underbrace{\begin{pmatrix} \dot{x} \\ x \\ D_x \\ \dot{y} \\ y \\ D_y \\ \dot{z} \\ z \\ D_z \end{pmatrix}}_y + B \begin{pmatrix} T \\ g \\ 0 \end{pmatrix}$$

$$\underbrace{\begin{pmatrix} \dot{x} \\ x \\ \dot{y} \\ y \\ \dot{z} \\ z \end{pmatrix}}_{\eta} = H \underbrace{\begin{pmatrix} \dot{x} \\ x \\ D_x \\ \dot{y} \\ y \\ D_y \\ \dot{z} \\ z \\ D_z \end{pmatrix}}_y$$

where y denotes the state vector, \dot{y} represents how the state vector varies over time, A is the state transition model, $B \begin{pmatrix} T \\ g \\ 0 \end{pmatrix}$ is the control input, η denotes the available measurements and H is the observation model. Matrices A , B and H are

$$A = \begin{pmatrix} 0 & 0 & -1/m & 0 & 0 & 0 & 0 & 0 & 0 \\ 1 & 0 & 0 & 0 & 0 & 0 & 0 & 0 & 0 \\ 0 & 0 & 0 & 0 & 0 & 0 & 0 & 0 & 0 \\ 0 & 0 & 0 & 0 & 0 & -1/m & 0 & 0 & 0 \\ 0 & 0 & 0 & 1 & 0 & 0 & 0 & 0 & 0 \\ 0 & 0 & 0 & 0 & 0 & 0 & 0 & 0 & 0 \\ 0 & 0 & 0 & 0 & 0 & 0 & 0 & 0 & -1/m \\ 0 & 0 & 0 & 0 & 0 & 0 & 1 & 0 & 0 \\ 0 & 0 & 0 & 0 & 0 & 0 & 0 & 0 & 0 \end{pmatrix}$$

$$B = \begin{pmatrix} C_\varphi S_\theta C_\phi + S_\varphi S_\phi & 0 & 0 \\ 0 & 0 & 0 \\ 0 & 0 & 0 \\ S_\varphi S_\theta C_\phi - C_\varphi S_\phi & 0 & 0 \\ 0 & 0 & 0 \\ 0 & 0 & 0 \\ 0 & 0 & 0 \\ C_\theta C_\phi & -1 & 0 \\ 0 & 0 & 0 \\ 0 & 0 & 0 \end{pmatrix}$$

$$H = \begin{pmatrix} 1 & 0 & 0 & 0 & 0 & 0 & 0 & 0 & 0 \\ 0 & 1 & 0 & 0 & 0 & 0 & 0 & 0 & 0 \\ 0 & 0 & 0 & 1 & 0 & 0 & 0 & 0 & 0 \\ 0 & 0 & 0 & 0 & 1 & 0 & 0 & 0 & 0 \\ 0 & 0 & 0 & 0 & 0 & 0 & 1 & 0 & 0 \\ 0 & 0 & 0 & 0 & 0 & 0 & 0 & 1 & 0 \end{pmatrix}$$

where m denotes total mass of the quadrotor.

The schematic of the Kalman filter used here is

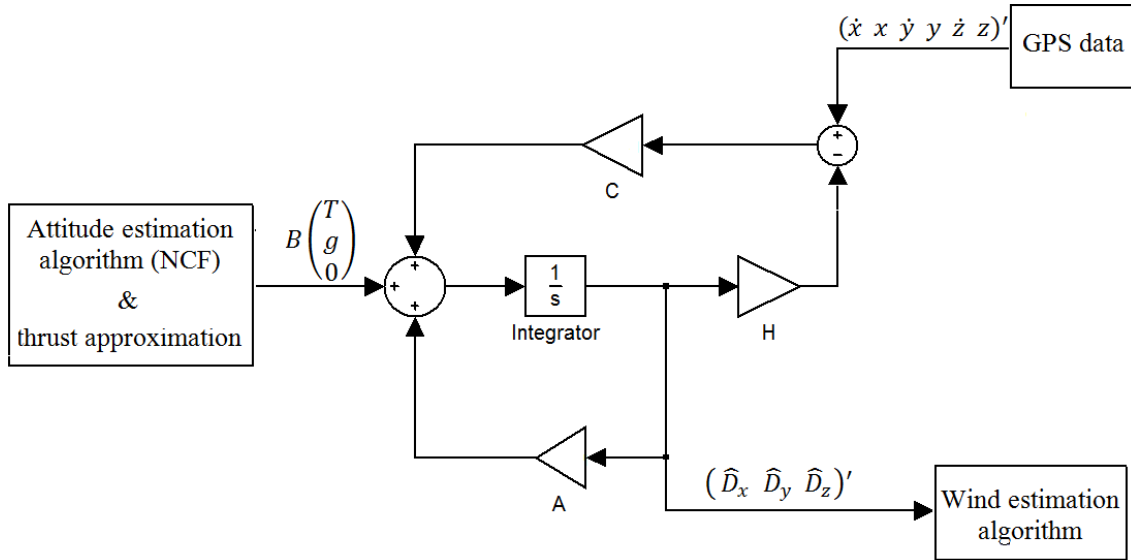


Figure 29: Kalman filter schematic for drag force estimation

where the blocks “Attitude estimation algorithm & thrust approximation” and “Wind estimation algorithm” make reference to the non-linear complementary filter implemented in the quadrotor (providing the Euler angles adopted by the quadrotor) and the thrust approximation explained in *Section 5.1.2.*, and to the algorithm showed in *Section 2.3.*, respectively. Additionally, matrix C represents the gain of the filter. The MatLab® function “*kalman*” has been used to compute this gain. Finally, the drag force used within the wind speed calculation algorithm is

$$D_{kalman} = \sqrt{\hat{D}_x^2 + \hat{D}_y^2}$$

It is expected to get a delay in the drag force estimation.

Chapter 6

Simulations, tests & measurements

6.1. Simulations

This section shows the validation of the methods used to estimate wind speed and direction. *Table 12* shows the settings of the System model and *Table 13* compares algorithms accuracy. *Figure 30* represents the scheme followed to validate the three methods and the wind speed estimation algorithm (same for the wind direction algorithm). Notice that the input “Turbulent wind vector” is known.

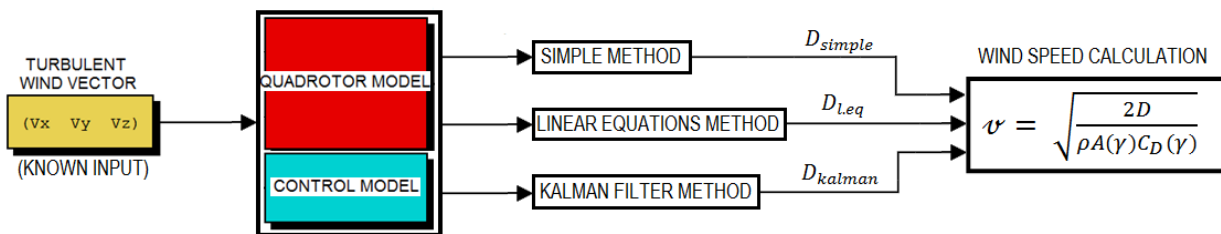


Figure 30: Scheme: methods and algorithms validation

Table 12: System model settings

Parameter	Value	Parameter	Value
Cx	0.9	g	9.81 m/s ²
A ₀	0.27354 m ²	m	1.15 kg
I _{xx}	0.02 kgm ²	l	0.27 m
I _{yy}	0.02 kgm ²	r	0.125 m
I _{zz}	0.04 kgm ²	P _s	1

Table 13: Relative error in % comparing methods

Wind Speed [m/s]	Wind speed estimation [m/s] - Simple, Linear equations & Kalman method	Error [%] - Simple, Linear equations & Kalman method
1	1.0012	0.12
2	2.0943	0.47
3	3.0324	1.08
4	4.0754	1.89
5	5.1443	2.89
6	6.2383	3.97
7	7.3509	5.01

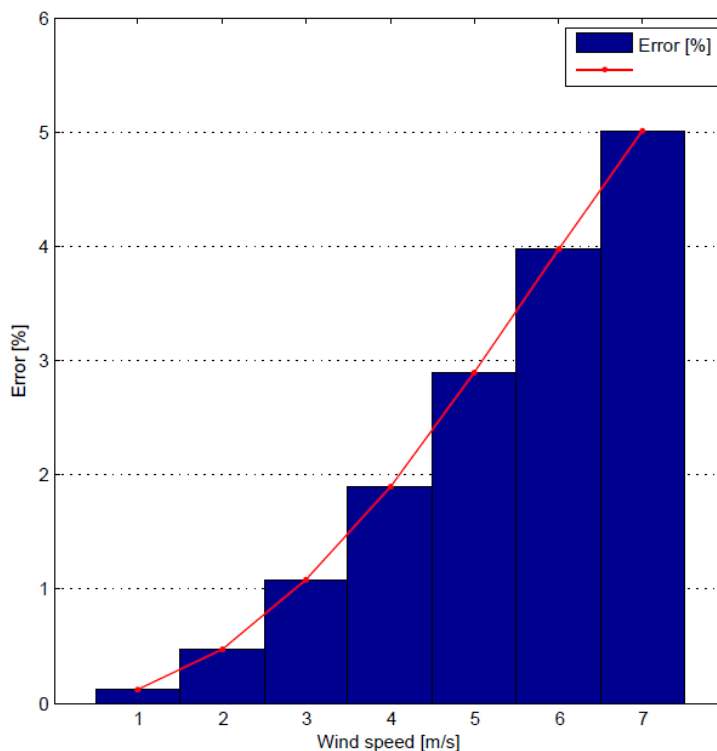


Figure 31: Relative error in % comparing methods

Under constant winds all three methods are valid, performing equally fine. Real wind profiles are not constant, even less turbulent winds. The methods are checked now for a turbulent wind profile along the X-axis generated with the software Bladed® (Figure 31)

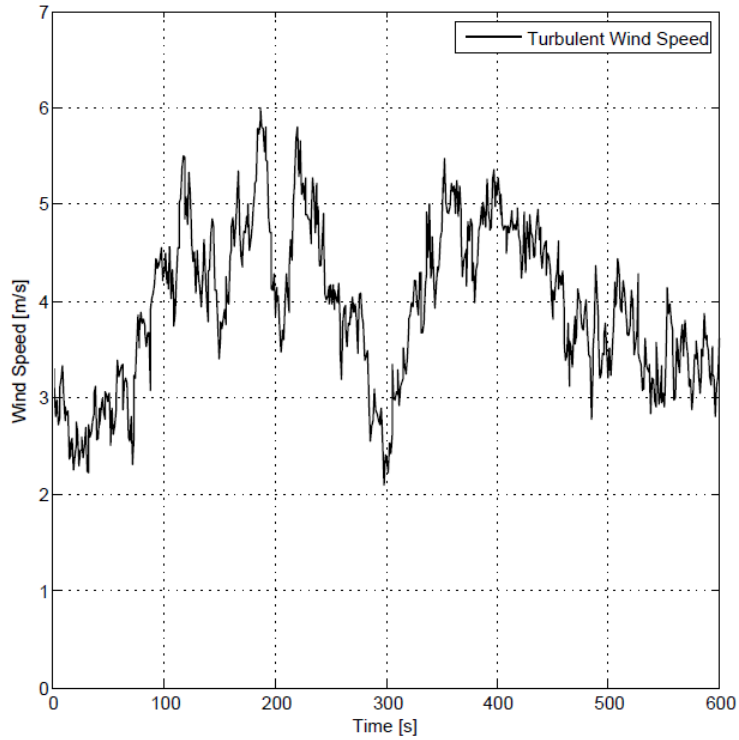


Figure 32: Turbulent wind profile generated using Bladed®

Drag force is estimated and wind vector is afterwards calculated using the algorithm derived in *Section 2.3*. Results are shown in *Figure 33*

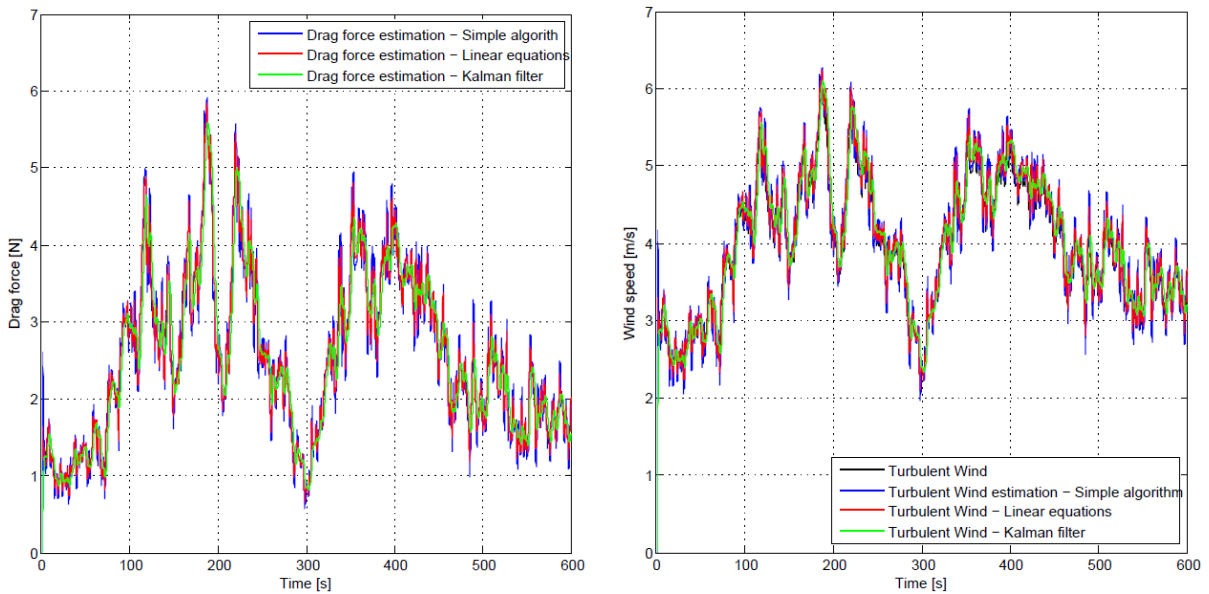


Figure 33: Drag force and wind speed comparison for turbulent simulated wind conditions along the X-axis

At first glance all 3 methods match the original turbulent. To determine the real performance of each method a detailed view of *Figure 33* is shown in *Figure 34*

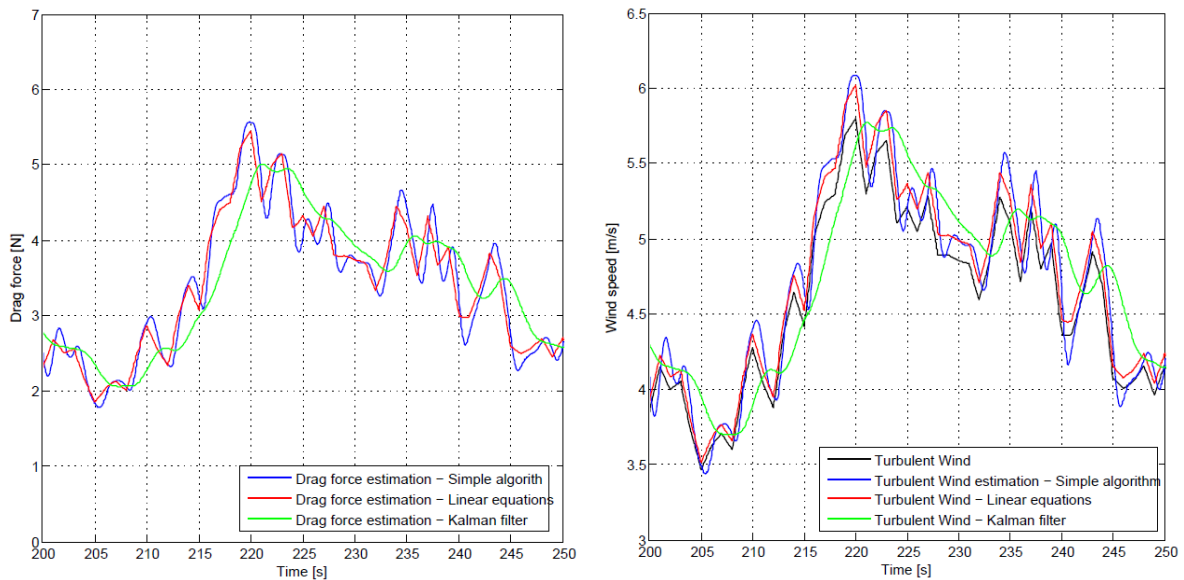


Figure 34: Detailed drag and wind speed comparison for turbulent simulated wind conditions along the X-axis

The estimation based on the simple method and the linear equations tend to overestimate and underestimate the wind speed during transients, when dynamic effects gain strength. On the contrary, the method based on the Kalman filter is not affected, giving a good response during the transients. This feature is especially interesting when using real data, considering that noise is always present in the measurements, especially in the data coming from the accelerometers. The Kalman filter is able to take into account noise coming from measurements to a certain extent, giving an even better response than the other two methods. This is shown in *Section 6.2*.

6.2. Tests

To validate the wind characterization algorithms with real data, several flight missions have been carried out. The chosen location for all outdoor and field missions is the SysTec facility in Fuldata-Rothwesten, at the outskirts of Kassel, Germany. The facility provides enough free space to fly safely, power connection and a meteorological mast to compare results. The fact that the owner of the land is the Fraunhofer Institute IWES makes possible to save much time in bureaucracy (flight permissions, insurance, etc). All indoor tests were carried out in the Fraunhofer Institute IWES office in Kassel.

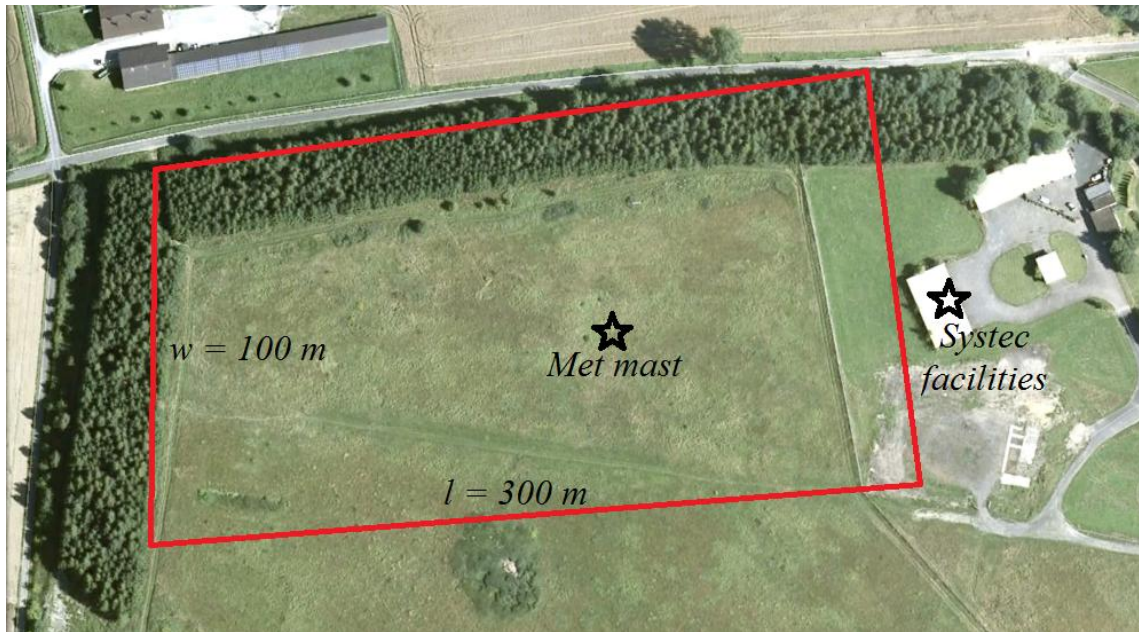


Figure 35: Satellite view of the field where measurement missions are carried out

6.2.1. Indoor tests

Before flying the quadrotor outdoors, indoor tests are necessary. The goal is to make sure that the whole system works properly, detecting any potential problems and solving them beforehand, avoiding setbacks during the field missions. The tasks are, namely

- Make sure that all parts are attached correctly, specially the propellers.
- Make sure that rotors spin in the right direction (two clockwise and two counter-clockwise). If at least one of the motors spins in the wrong direction the quadrotor will not takeoff.
- Calibrate IMU and RC channels.
- Make sure that the quadrotor reacts appropriately to the radio signals coming from the RC controller.
- Check the proper operation of the telemetry system and the data storage system. The telemetry system allows to visualize most of the relevant data on real-time. On the other hand, the data storage system creates log files, where all the flight data is stored for later analysis.
- Becoming familiar with the GCS.

6.2.2. Outdoor tests

After checking the basic operation of the quadrotor indoors, outdoors tests allow the controller to feel comfortable with the quadrotor dynamics during flight as well as with the RC controller. Besides, the autopilot control gains can be adjusted to get a better performance during flight (for instance, a more stable loitering mode) and additional issues that cannot be detected during the indoor test can subsequently be

solved. Before carrying out outdoor missions, batteries and RC controller must be fully charged. Furthermore, the team should have enough spare parts and the appropriate tools to replace or repair the most common breakdowns (for instance, broken propeller and broken landing part). Also, extra batteries and a LiPo battery charger are needed.

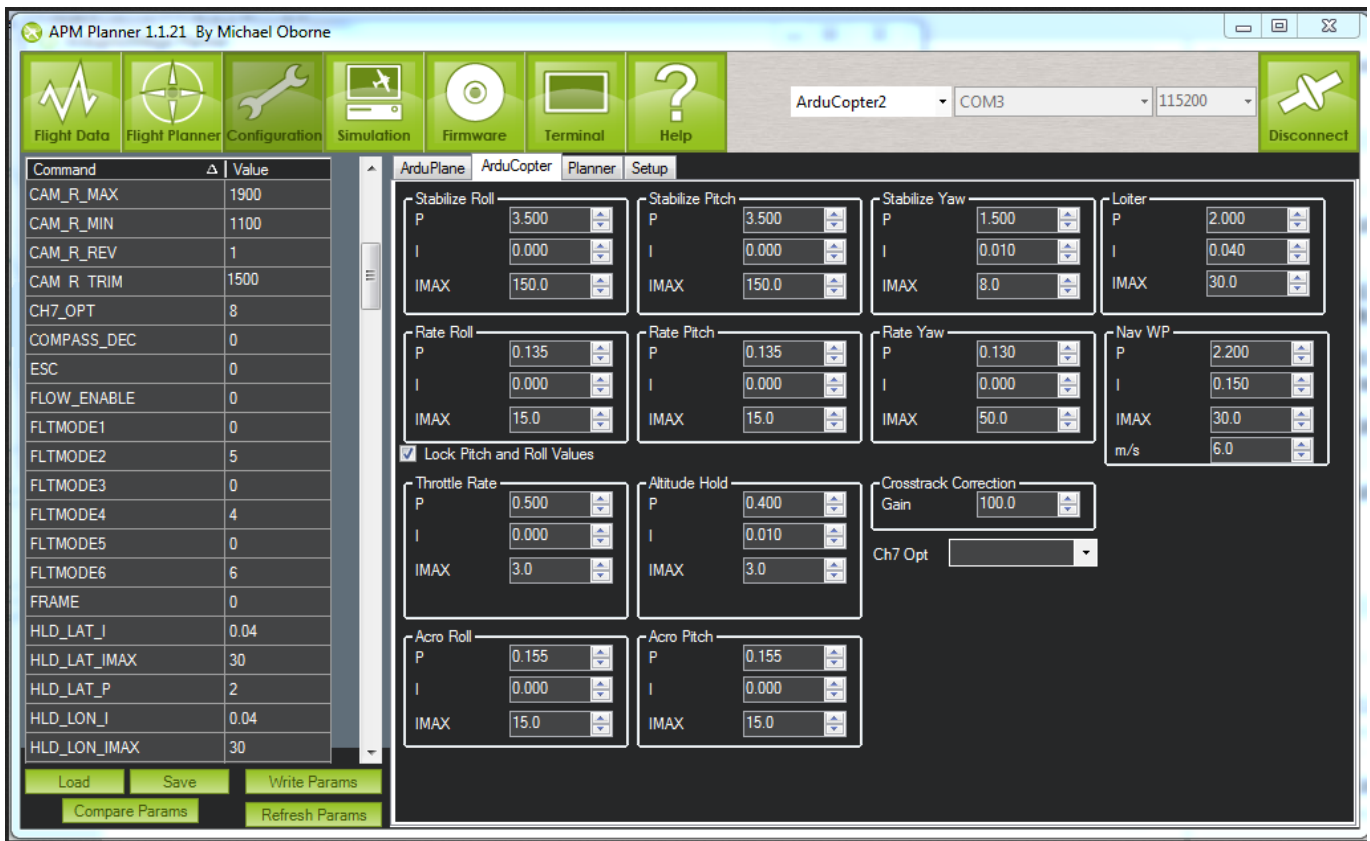


Figure 36: Screenshot of the PID setting configuration from the APM Planner 1.1.23 (Ground Control Station)

One of the problems encountered was the malfunction of the barometer. The reason was found to be the high humidity present in the air. Under humid conditions, the barometer chip cannot measure the absolute altitude properly. This issue is solved by covering the chip with a tissue or a soft sponge.

6.3. Field measurements

Two different measurement missions have been planned.

- In the first mission the quadrotor is flown under wind conditions and the results are compared to an external measurement device mounted on a meteorological mast at the same height than the loitering quadrotor. The expectation is to get a wind speed and direction in fairly good agreement with the data reported by the anemometer. Euler angles estimated by the flight controller algorithm (NCF) are assumed to have very little errors [33] and thus, they are considered error-free. On the other hand, accelerations signals are known to be very noisy. Due to this fact, it is expected that the linear

equations method for drag force calculation will give wrong results, so it may be necessary to low-pass filter the accelerometer signals to improve its performance. Additionally, the anemometer is considered to be an ideal measurement instrument giving the true speed and direction of the wind with 1 Hz time resolution.

- The second mission attempts to determine the performance of the algorithms under no wind conditions. Inaccuracies coming mainly from GPS, gyroscopes and accelerometers are taken into account by the autopilot system to a certain extent. The PID controller is in charge of satisfying the restrictions imposed by the RC controller (for instance, loitering or altitude hold) but inaccuracies make the controller to continuously correct the position, causing changes in attitude, even under no wind conditions. For this reason it is expected that the algorithm will report a low random wind speed spread over 360°.

Good synchronization with the met mast is necessary to compare results. Both quadrotor and met mast follow the Coordinated Universal Time (UTC). The quadrotor stores this time together with the rest of the parameters, making easier to coordinate both measurement systems and to compare results.

The scheme followed to calculate wind speed (same for wind direction) is shown in Figure 37. Notice that now the input “Turbulent wind vector” is unknown.

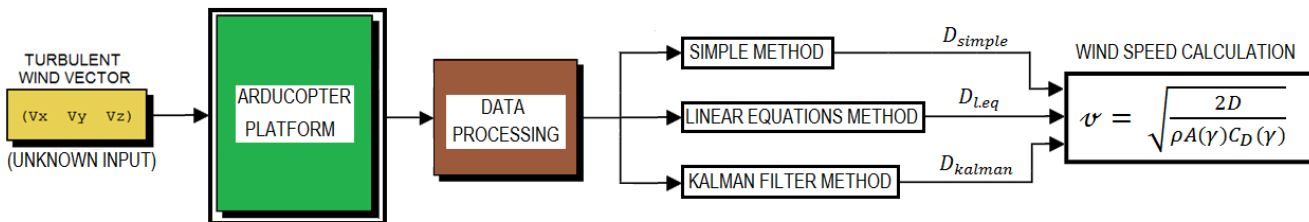


Figure 37: Scheme: wind speed calculation

6.3.1. Wind conditions

This measurement takes place on November the 9th, 2012 at the SysTec facility. The flight time at which the quadrotor loiters and provides useful data lasts 70 seconds. Unfortunately, access to the 1 Hz time resolution data from the anemometer was not possible. Instead, 5 minutes averages for wind speed and direction were provided. This fact limits the comparison possibilities between the three different drag force calculation methods, since no dynamic effects can be taken into account with only 5 minutes wind averages. However, the wind profile at the SysTec location is not turbulent at medium altitudes, especially with southern winds (from south to north), which is the case. Considering this, mean values can be compared relatively safely. Euler angles are computed by the flight controller and the rest of the parameters are estimated following the equation shown in Section 5.1.

The following table shows the minimum, maximum and mean values of wind speed and direction at the time the measurement mission took place, as well as the standard deviation. The wind direction is measured from the magnetic North.

Table 14: Statistics for wind profile measured by the meteorological mast

Parameter	Mean	Maximum	Minimum	Standard deviation
Wind speed [m/s]	4.6	6.2	2.6	0.8
Wind direction [°]	187	228	151	1.2

The angles adopted by the quadrotor during the measurement mission are the following

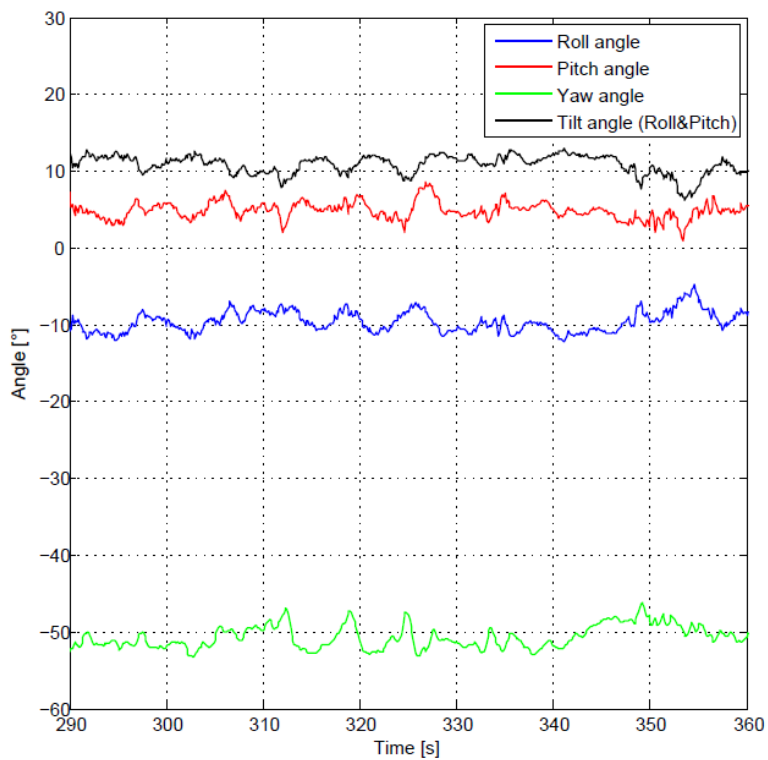


Figure 38: Quadrotor attitude during field measurement, reported by the flight controller

From these angles, the three methods are used to compute drag force acting on the quadrotor. As previously expected, noise coming from the accelerometers signal has a large effect on the method that uses the dynamic linear equations. The simple method and the Kalman filter method are almost unaffected by this phenomena. *Figure 39* shows a comparison between methods.

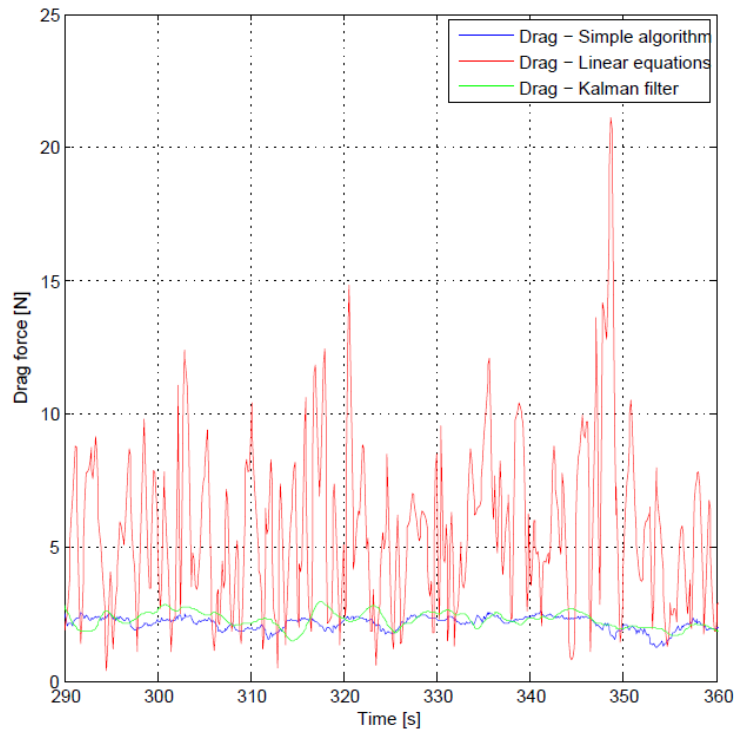


Figure 39: Drag force estimation. Accelerometer data is not filtered

In order to improve the performance of the second method, the accelerometer outputs have been low-pass filtered. The type of filter chosen is a 5th order Butterworth filter with normalized cutoff frequency 0.01. After filtering out the undesired high frequency content, the new drag force results as follows

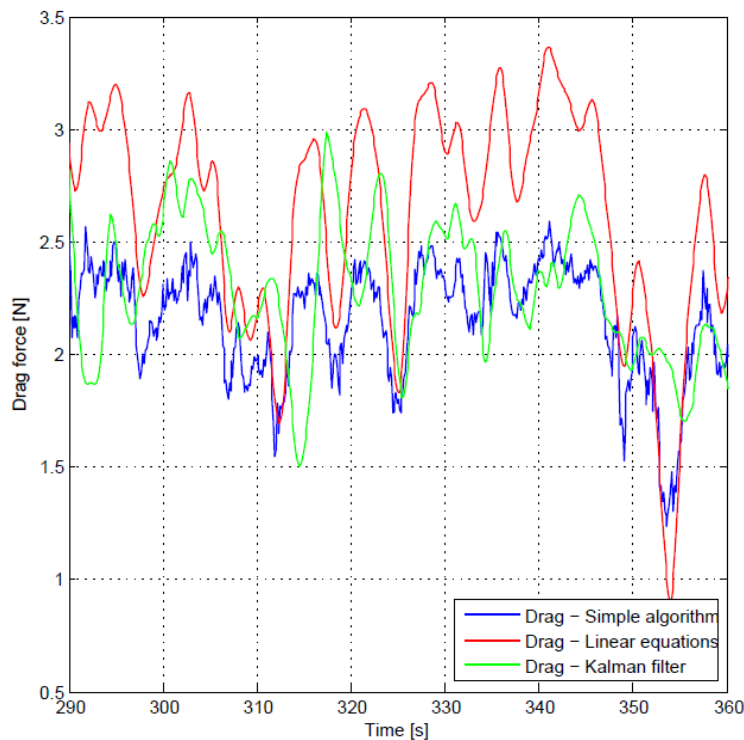


Figure 40: Drag force estimation. Accelerometer data is filtered

All three methods report a drag force mean value in the same order of magnitude. The performance of the method using the dynamic linear equation is still clearly affected by the accelerometers noise. On the other hand, the simple method reflects every up and down in the angles, while the Kalman filter method follows a smoother trajectory.

Now that drag forces are known, the wind equation can be solved and a comparison with the anemometer wind measurements can be done. The following two figures show the results obtained for wind speed and wind direction.

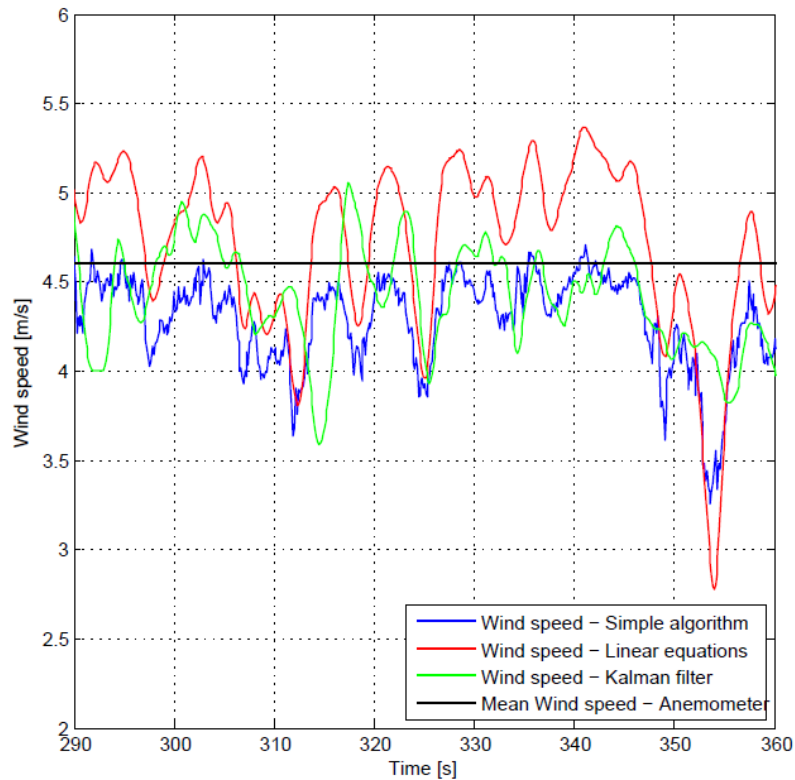


Figure 41: Wind speed estimation. Comparison with mean value of met mast measurement

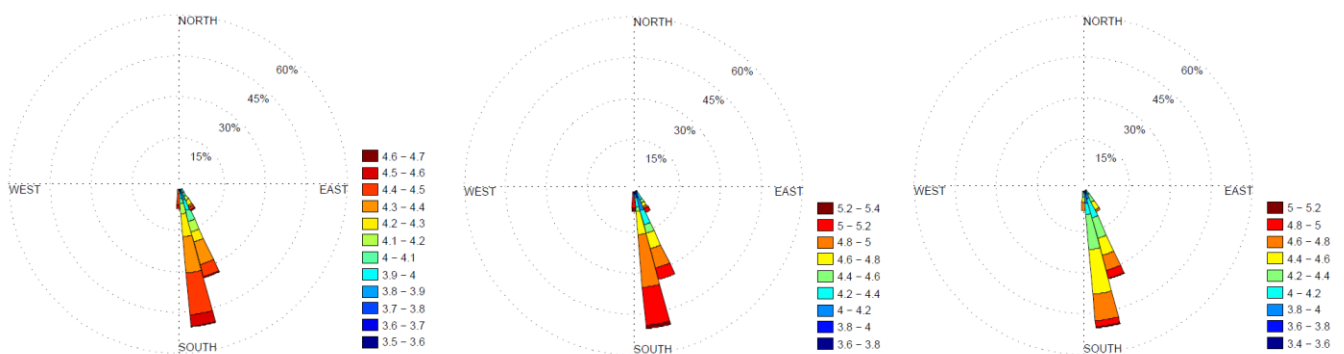


Figure 42: Wind rose. From left to right: Simple method, Linear equations method and Kalman filter method

6.3.2. No wind conditions

The purpose of this mission is to determine the response of the quadrotor under no wind conditions. The measurement lasts 25 seconds and it took place also at the SysTec facility. This time, accelerometers signals have been pre-filtered before using them on the second method. As expected, *Figures 36 and 37* show low random values of wind speed spread in all directions.

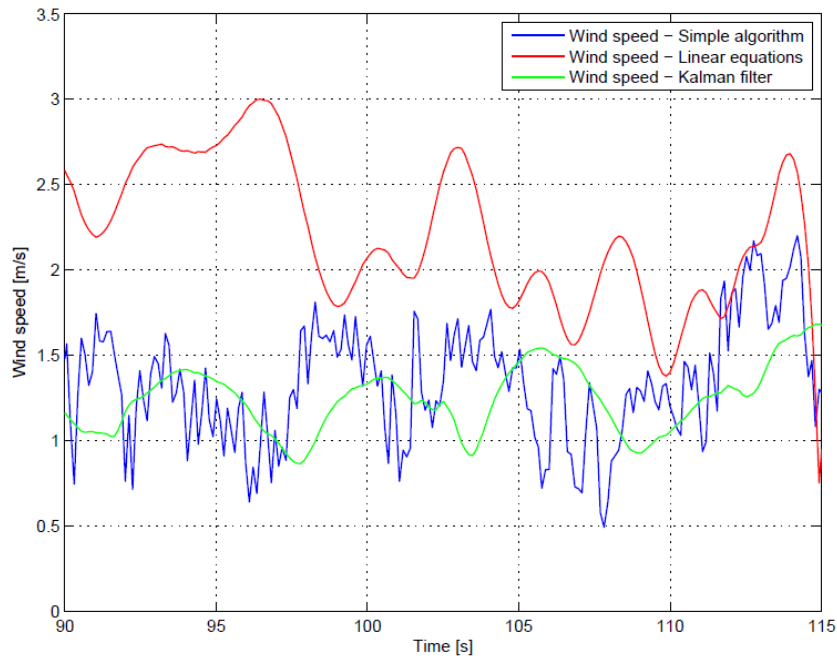


Figure 43: Wind speed estimation under no wind conditions

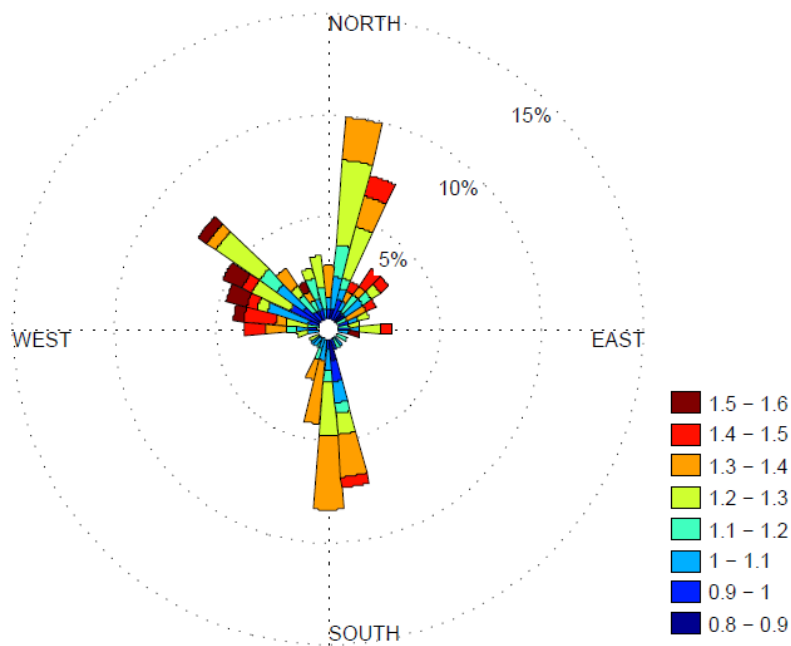


Figure 44: Wind rose under no wind conditions – Simple method estimation

Even though the results are the expected, they indicate that the algorithm generates wrong estimations when no wind or light breeze is present.

6.4. Results

As shown in *Figure 41*, wind speeds calculated are in fairly good agreement with the data reported by the anemometer, suggesting that the algorithm derived from the dynamic pressure equation can be used. As far as wind direction is concerned, results show that the quadrotor was indeed tilting against the incoming wind and that the approach followed to compute the wind direction works properly. Statistics for wind profile estimation are compared to the anemometer data in *Table 15*

Table 15: Statistics for wind profile estimation

	Wind speed		Wind direction	
	Mean [m/s]	Standard deviation	Mean [°]	Standard deviation
Anemometer	4.6	0.8	187	1.2
Simple algorithm	4.287	0.264	195	7.07
Linear equations	4.71	0.477	195	7.07
Kalman filter	4.41	0.297	195	7.07

Mean values for both wind speed and wind direction are very similar and standard deviations are small enough (in comparison to their respective mean values) to think that the mean represents the observed data quite well. However, time intervals for anemometer and quadrotor are not the same. The first one lasts 5 minutes while the second one only 1.17 minutes, meaning that comparison conclusions must be taken cautiously.

Regarding no wind conditions, the quadrotor instability misleads the wind estimation algorithm, leading into wrong wind profile estimation. As a result, the current platform should only be used to determine well defined wind profiles.

Chapter 7

Conclusions, limitations & future projects

7.1. Conclusions

The project proves the feasibility of a quadrotor as a measurement instrument itself, with no dedicated wind sensors on board. The suggested platform as well as the algorithms seems to relate quadrotor attitude to wind profile successfully, obtaining good wind profile estimations. The current platform performs well under wind conditions but cannot characterize light random wind, providing the algorithm wrong wind estimations.

A model of the platform has been developed in Simulink®, divided into a mechanical submodel, an aerodynamic submodel, a motors submodel and a control submodel. The whole model has been used to simulate the real system and validate the applicability of the wind profile estimation algorithms under ideal conditions. Wind estimations have been carried out following three different approaches, two of them taking into account dynamic effects and the other without doing it. The performance of the Simulink® model is satisfactory, being able to handle simulated winds up to 10 m/s. Faster winds can be handled by adjusting the PID gains of the controller. Finally, several measurement campaigns have been carried out, getting useful data from the selected platform. This data is analyzed and processed via MatLab/Simulink®, which makes possible to use the estimation algorithms and to get a wind speed and wind direction in fair agreement with the data provided by an anemometer, considering this as an ideal sensor with no errors.

7.2. Limitations

The small angle assumption used within the control model limits its performance. Furthermore, noise coming from the sensors is not considered in the model. Also, physical properties and aerodynamic coefficients such as moments of inertia and drag coefficient are assumed, limiting the accuracy of the model

Concerning the wind estimation algorithm, its limitation depends on the drag force calculation method applied. The simple method does not take into account dynamic effects. It will give wrong estimation during transients and thus, should only be used under steady conditions. The second method is strongly affected by accelerometers noise. It should not be used if the signals are not low-pass filtered. The third method seems to have fewer weaknesses, but its performance while coping with transients could not be demonstrated.

Concerning the comparison between met mast data and wind estimation, only 5 minutes averages were available and not 1 Hz time series. This fact has been found to be a big limitation in order to determine performance of the wind estimation algorithm during transients and time resolution of the platform.

7.3. Future projects

Further measurement missions should be carried out in order to determine spatial and time resolution of the system. Tests in wind tunnels are required to get a better knowledge of the aerodynamic behavior. The installation of ammeters and voltmeters on each motor would provide extra variables, that fed back via telemetry system to the GCS could help to improve the average performance of the wind estimation algorithm as well as supplying an additional method for attitude estimation, as shown in *Section 3.2.3*.

Concerning applicability of the system, a new research could focus on the use of several quadrotors that, acting as an organized swarm, would be able to generate a 3D representation of the wind profile. When located within a wind farm, the swarm could create a virtual grid between turbines, measuring wake interactions and their progress in time and space.

Also, further studies could analyze the applicability and performance of the system on offshore locations. A network of very cost effective “meteorological mast” could be virtually built. Here especial attention should be paid concerning measurement procedures and safety rules.

Chapter 7

References

- [1] - Rohde R, Muller RA, Jacobsen R, Muller E, Perlmutter S, et al. (2013) *A New Estimate of the Average Earth Surface Land Temperature Spanning 1753 to 2011*. Geoinfor Geostat: An Overview 1:1.. doi:10.4172/gigs.1000101
- [2] - Hansen, J., Mki. Sato, and R. Ruedy, 2012: *Perception of climate change*. *Proc. Natl. Acad. Sci.*, 109, 14726-14727, E2415-E2423, doi:10.1073/pnas.1205276109
- [3] - Vestas: *VI64-8.0 MW*. Available online at <http://www.vestas.com/en/wind-power-plants/procurement/turbine-overview/v164-8.0-mw-offshore.aspx#/vestas-univers>.
- [4] - EWEA - Sixth framework project (2011): *Design limits and solutions for very large wind turbines*. Flow. With assistance of Rebecca Barthelmie (UpWind). Available online at http://www.ewea.org/fileadmin/ewea_documents/documents/upwind/21895_UpWind_Report_1ow_web.pdf.
- [5] – Gryning, Sven-Erik; Batchvarova, Ekaterina; Brümmer, Burghard; Jørgensen, Hans; Larsen, Søren (2007): *On the extension of the wind profile over homogeneous terrain beyond the surface boundary layer*. In *Boundary-Layer Meteorology* 124 (2), pp. 251–268. Available online at <http://dx.doi.org/10.1007/s10546-007-9166-9>.
- [6] – Lange, Bernhard; Højstrup, Jørgen (2001): *Evaluation of the wind-resource estimation program WASP for offshore applications*. In *10th International Conference on Wind Engineering* 89 (3–4), pp. 271–291. Available online at <http://www.sciencedirect.com/science/article/pii/S0167610500000829>.
- [7] - Giebel, Gregor; Schmidt Paulsen, Uwe; Bange, Jens; La Cour-Harbo, Anders; Reuder, Joachim; Mayer, Stephanie et al. (2012): *Autonomous Aerial Sensors for Wind Power Meteorology - A Pre-Project*. (Denmark. Forskningscenter Risoe. Risoe-R). Available online at http://vbn.aau.dk/files/60873544/PSOAerialSensors_FinalReport.pdf.
- [8] - Joachim Reuder; Pascal Brisset; Marius Müller Jonassen; Stephanie Mayer (2009): *The Small Unmanned Meteorological Observer SUMO: A new tool for atmospheric boundary layer research*. In *Meteorologische Zeitschrift* 18 (2), pp. 141–147. Available online at <http://dx.doi.org/10.1127/0941-2948/2009/0363>.
- [9] - Hendrick, F.; Rozanov, A.; Johnston, P. V.; Bovensmann, H.; Mazière, M. de; Fayt, C. et al. (2010): *Meteorological profiling of the lower troposphere using the research UAV "M2AV Carolo"*. In *Atmos. Meas. Tech. Discuss.* 3 (6), pp. 5179–5209. Available online at <http://www.atmos-meas-tech-discuss.net/3/5179/2010/>.

- [10] - Wildmann, Norman (2011): *Measurement of the structures and processes in the atmospheric boundary layer during the late-afternoon transition using the recently developed research UAV 'MASC', including the comparison with other UAV organised in COST Action ES 0802*. Available online at http://bllast.sedoo.fr/documents/reports/UAS/BLLAST_UAS_COST-es0802_report_20110802_Wildmann.pdf.
- [11] - *Boudary Layer Late Afternoon and Sunset Turbulence (BLLAST)*. Available online at <http://bllast.sedoo.fr/campaigns/2011/>.
- [12] - Stephan Barth; Holger Koch; Achim Kittel; Joachim Peinke; Jorg Burgold; Helmut Wurmus (2005): *Laser-cantilever anemometer: A new high-resolution sensor for air and liquid flows*. In *Review of Scientific Instruments* 76 (7), p. 75110. Available online at <http://link.aip.org/link/?RSI/76/075110/1>.
- [13] - Mansour, M.; Kocer, G.; Lenherr, C.; Chokani, N.; Abhari, R. S. (2011): *Seven-Sensor Fast-Response Probe for Full-Scale Wind Turbine Flowfield Measurements* 133 (8). Available online at <http://gasturbinespower.asmedigitalcollection.asme.org/article.aspx?articleid=1428610>.
- [14] - White, Frank M. (2003): *Fluid mechanics*. 5. ed., International ed. Boston [u.a.]: McGraw-Hill (McGraw-Hill series in mechanical engineering)
- [15] - Marchiori, Andrea (2012): *Unmanned Aerial Vehicle (Quadrotor Helicopter) for Aerial Wind Measurement*.
- [16] - Austin, Reg (2010): *Unmanned air vehicles. UAV design, development, and deployment*. Chichester, West Sussex, U.K, Hoboken, NJ: Wiley.
- [17] - Ehredt, Dave: NATO - Joint Air Power Competence Centre. In *UAS Yearbook - UAS: The Global Perspective*. Available online at http://uas.usgs.gov/UAS-Yearbook2010/pdf/P061-062_NATO_Dave-Ehredt.pdf.
- [18] - Ritz, R.; Mueller, M.; D'Andrea, R. (2012): *Cooperative Quadrocopter Ball Throwing and Catching*. In : IEEE/RSJ International Conference on Intelligent Robots and Systems. IEEE, pp. 4972–4978.
- [19] - *Why Quadrotors are so Popular for Research?* (2012). Available online at <http://www.quadrotors.net/why-quadrotors-are-so-popular-for-research/>.
- [20] - Mahony, R.; Kumar, V.; Corke, P. (2012). In *Robotics Automation Magazine, IEEE: Multirotor Aerial Vehicles: Modeling, Estimation, and Control of Quadrotor* 19 (3), pp. 20–32. Available online at <http://ieeexplore.ieee.org/xpl/articleDetails.jsp?reload=true&arnumber=6289431>.
- [21] – Jaw-KuenShiau; Chen-Xuan Huang; Ming-Yu Chang (2012): *Noise Characteristics of MEMS Gyro's Null Drift and Temperature Compensation*. In *Journal of Applied Science and Engineering* 15 (3), pp. 239–246. Available online at <http://www2.tku.edu.tw/~tkjse/15-3/04-AE10102.pdf>.
- [22] – Esfandyari, Jay; Nuccio, Roberto de; Gang Xu (2010): *Introduction to MEMS gyroscopes*. SolidState Technologies. Available online at <http://www.electroiq.com/articles/stm/2010/11/introduction-to-mems-gyroscopes.html>.

- [23] – Nasiri, Steven: *A Critical Review of MEMS Gyroscopes Technology and Commercialization Status*. InvenSense. Available online at <http://invensense.com/mems/gyro/documents/whitepapers/MEMSGyroComp.pdf>.
- [24] – Chollet, Franck; Liu, Haobing (2010): *A (not so) short introduction to MEMS*. 4th ed. Available online at <http://memscyclopedia.org/Document/introMEMS.pdf>.
- [25] – Andrejaši, Matej (2008): *MEMS accelerometers*, 2008. Available online at http://mafija.fmf.uni-lj.si/seminar/files/2007_2008/MEMS_accelerometers-koncna.pdf.
- [26] – Kong Wai Weng (2009): *Measuring tilt angle with a gyro and accelerometer*. In *Robot Head to Toe Magazine* 1. Available online at <http://tutorial.cytron.com.my/2012/01/10/measuring-tilt-angle-with-gyro-and-accelerometer/>.
- [27] – Chee, W. (2001): *Measuring Yaw Rate with Accelerometers* (SAE Technical Paper 2001-01-2535). Available online at <http://papers.sae.org/2001-01-2535/>.
- [28] – Gross, Bob (2013): *MaxSonar operation on a multi-copter*. MaxBotix. Available online at <http://www.maxbotix.com/articles/067.htm>.
- [29] – *XL-MaxSonar- EZ Series*. Available online at http://maxbotix.com/documents/XL-MaxSonar-EZ_Datasheet.pdf.
- [30] – Young-Soo Suh (2003). In : *Science and Technology, 2003. Proceedings KORUS 2003. The 7th Korea-Russia International Symposium: Attitude estimation using low cost accelerometer and gyroscope*, vol. 2, pp. 423-427 vol.2.
- [31] - Maybeck, Peter S. (1982): *Stochastic models, estimation and control*. A series of monographs and textbooks. New York [u.a.]: Acad. Press (Mathematics in science and engineering, 141,2)
- [32] – Hong, Sung Kyung; Park, Sungsu (2008): *Minimal-Drift Heading Measurement using a MEMS Gyro for Indoor Mobile Robots*. In *Sensors* 8 (11), pp. 7287–7299. Available online at <http://www.mdpi.com/1424-8220/8/11/7287>.
- [33] – Hyon Lim; Jaemann Park; Daewon Lee; Kim, H. J. (2012). In *Robotics Automation Magazine, IEEE: Build Your Own Quadrotor: Open-Source Projects on Unmanned Aerial Vehicles* 19 (3), pp. 33–45.
- [34] - *Intelligent Robots and Systems, 2008. IROS 2008. IEEE/RSJ International Conference: A complementary filter for attitude estimation of a fixed-wing UAV* (2008).
- [35] – Premerlani, William; Bizard, Paul (2009): *Direction Cosine Matrix IMU: Theory*. Available online at gentlenav.googlecode.com/files/DCMDraft2.pdf.
- [36] - InvenSense (2012): *MPU-6000 and MPU-6050 Product Specification*. InvenSense. Available online at <http://www.invensense.com/mems/gyro/documents/PS-MPU-6000A.pdf>.
- [37]- InvenSense (2008): *Integrates Dual-Axis Gyro IDG-500*. InvenSense. Available online at http://www.sparkfun.com/datasheets/Components/SMD/Datasheet_IDG500.pdf.
- [38] - InvenSense (2010): *ISZ-500 Single-Axis Z-Gyro Product Specification*. InvenSense. Available online at <http://www.invensense.com/mems/gyro/documents/PS-ISZ-0500B.pdf>.

- [39] - Analog Devices: *ADXRS610 Product Specification*. Analog Devices. Available online at http://www.analog.com/static/imported-files/data_sheets/ADXRS610.pdf.
- [40] - InvenSense (2010): *ITG-3200 3-Axis Gyro Evaluation Board Application Note Rev 1.1*. InvenSense. Available online at <http://invensense.com/mems/gyro/documents/EB-ITG-3200-00-01.1.pdf>.
- [41] - HoneyWell. *3-Axis Digital Compass IC HMC5883L*. HoneyWell. Available online at http://www51.honeywell.com/aero/common/documents/myaerospacecatalog-documents/Defense_Brochures-documents/HMC5883L_3-Axis_Digital_Compass_IC.pdf.
- [42] - HoneyWell: *3-Axis Digital Compass IC HMC5843*. HoneyWell. Available online at http://www51.honeywell.com/aero/common/documents/myaerospacecatalog-documents/Defense_Brochures-documents/HMC5843.pdf.
- [43] - Philips Semiconductors (2000): *KMZ51 - Magnetic field sensor*. Philips. Available online at http://www.datasheetcatalog.org/datasheet/philips/KMZ51_3.pdf.
- [44] - Measurement Specialities (2012): *MS5611 - 01BA03*. Available online at <http://www.meas-spec.com/downloads/MS5611-01BA03.pdf>.
- [45] - Freescale Semiconductors (2006): *Integrated Silicon Pressure Sensor Altimeter/Barometer Pressure Sensor On-Chip Signal Conditioned, Temperature Compensated and Calibrated*. Available online at http://www.freescale.com/files/sensors/doc/data_sheet/MPX4115.pdf.
- [46] - Bosch Sensortec (2011): *BMP085 - Digital pressure sensor*. Bosch. Available online at <http://dlnmh9ip6v2uc.cloudfront.net/datasheets/Sensors/Pressure/BST-BMP085-DS000-06.pdf>.
- [47] - Analog Devices (2007): *Small, Low Power, 3-Axis $\pm 3g$ i MEMS Accelerometer - ADXL330*. Analog Devices. Available online at http://www.analog.com/static/imported-files/data_sheets/ADXL330.pdf.
- [48] - Analog Devices: *3 - Axis Digital Accelerometer - ADXL345*. Analog Devices. Available online at http://www.analog.com/static/imported-files/data_sheets/ADXL345.pdf.
- [49] - Bosch Sensortec (2010): *BMA180 - Digital, triaxial acceleration sensor*. Bosch. Available online at <http://jp.bosch-sensortec.com/content/language1/downloads/BST-BMA180-FL000-03.pdf>.
- [50] - STMicroelectronics (2008): *LIS344ALH - MEMS inertial sensor high performance 3-axis $\pm 2/\pm 6g$ ultracompact linear accelerometer*. STMicroelectronics. Available online at <http://www.st.com/st-web-ui/static/active/en/resource/technical/document/datasheet/CD00182781.pdf>.
- [51] – MikroKopter: *FlightCtrl License*. Available online at <http://svn.mikrokopter.de/filedetails.php?rename=FlightCtrl&path=%20LICENSE.TXT>.
- [52] – APC Propellers: *APC Suggested RPM Limits*. Available online at http://www.apcprop.com/v/html/rpm_limits.html.
- [53] - Babuska, Robert; Stramigiolo, Stefano (1999): *MatLab and Simulink for Modeling and Control*, Control Laboratory, Delft University of Technology. Available online at <http://www.dcsc.tudelft.nl/~sc4070/transp/refresher.pdf>

[54] - Luukkonen, Teppo (2011): *Modelling and control of quadcopter*, Independent research project in applied mathematics, School of Science, Aalto University. Available online at <http://sal.aalto.fi/publications/pdf-files/eluu11.pdf>

Appendix

Budget & project schedule

Budget

The budget gives an idea of the project cost estimate. It is divided into two parts. The first one makes reference to the equipment or materials that had to be purchased for the correct development of the project. The second part refers to the cost of engineering-hour and other incomes.

Table 16: Budget spent in platform, materials and other equipment.

	Items	Number	Unitary cost	Total cost [€]
Platform	ArduCopter 3DR Quad - Ready to Fly -w/ APM2.5	1 u.	635.9 €	635.10 €
	3DR Radio Telemetry Kit 433 Mhz	1 u.	91.51 €	91.52 €
	MB1200 Sonar	1 u.	43.76 €	43.77 €
Radio Control	Spektrum DX8 Tx/Rx	1 u.	342.21 €	342.22 €
Batteries	Turnigy 3000mAh 3S 40C Lipo Pack	2 u.	24.15 €	48.30 €
Battery charger	Turnigy Accucel-6 50W 6A Balancer/Charger w/ accessories	1 u.	30.14 €	30,14 €
Spare parts	APC SlowFly Propeller 10x4.7 SF	4 u.	4.2 €	16.8 €
	APC SlowFly Propeller 10x4.7 SFP	4 u.	5.1 €	20.40 €
	XT60-Deans battery adapter	2 u.	2.99 €	5.98 €
	Motor AC2830-358, 850Kv	2 u.	13.56 €	27.12 €
Total Shipping rate	FedEx International Priority			71.90 €
Total (VAT included)				1334.05 €

Table 17: Budget spent in human resources.

	Concept	Number	Unitary cost	Total cost [€]
Salary	Cost of Engineer-hour	240 hours	7.5 €	1.800 €
Extras	Scholarship	6 months	400 €	2.400 €
Total (VAT included)				4.200 €

Project schedule

Table 18: Project schedule

	Task name	Duration	Start	Finish	Predecessors
1	Setting objectives	3 days	01/08/2012 8:00	03/08/2012 17:00	
2	Defining project requirements	3 days	06/08/2012 8:00	08/08/2012 17:00	1
3	Studying platforms considered	14 days	09/08/2012 8:00	28/08/2012 17:00	2
4	Platform selection	8 days	29/08/2012 8:00	07/09/2012 17:00	3
5	Platform purchase order	0 days	07/09/2012 17:00	07/09/2012 17:00	4;21
6	Obtaining flight permissions	4 days	10/09/2012 8:00	13/09/2012 17:00	5
7	Contacting Met-Mast team	2 days	14/09/2012 8:00	17/09/2012 17:00	6
8	Plannifying outdoor flight missions	2 days	10/09/2012 8:00	11/09/2012 17:00	5
9	Flight missions GREEN LIGHT	0 days	17/09/2012 17:00	17/09/2012 17:00	7
10	Platform arrival	0 days	03/10/2012 17:00	03/10/2012 17:00	5FS+18 days
11	Checking telemetry system	3 days	04/10/2012 8:00	08/10/2012 17:00	10
12	Understanding platform data acquisition	4 days	09/10/2012 8:00	12/10/2012 17:00	11
13	Scripts development for transferring data between GCS & MatLab/Simulink	20 days	15/10/2012 8:00	09/11/2012 17:00	12;18
14	Flying missions - Obtaining real data	20 days	12/11/2012 8:00	07/12/2012 17:00	13
15	Data pre-processing	16 days	10/12/2012 8:00	07/01/2013 17:00	14
16	Analysis & results	12 days	08/01/2013 8:00	23/01/2013 17:00	15
17	Developing wind profile characterization algorithms	6 days	06/08/2012 8:00	13/08/2012 17:00	1
18	Implementing algorithms into MatLab/Simulink	8 days	02/10/2012 8:00	11/10/2012 17:00	17;20
19	Quadrotor dynamics study	10 days	09/08/2012 8:00	22/08/2012 17:00	2
20	Modelling platform in MatLab/Simulink	28 days	23/08/2012 8:00	01/10/2012 17:00	19
21	Power source study (Cable vs. Battery)	8 days	09/08/2012 8:00	20/08/2012 17:00	2
22	Flight time study	6 days	21/08/2012 8:00	28/08/2012 17:00	21

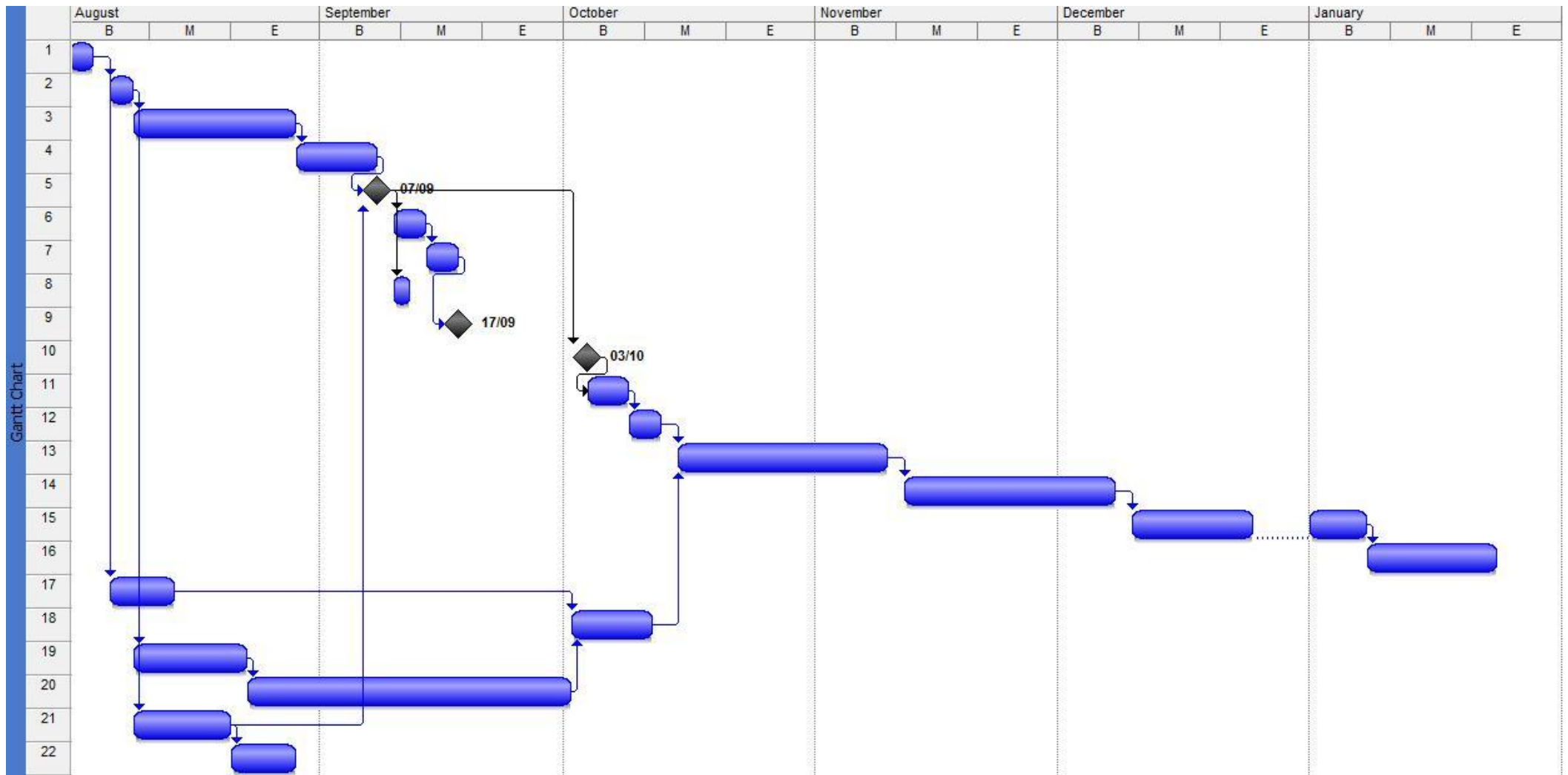


Figure 45: Gantt diagram